Journal Pre-proof

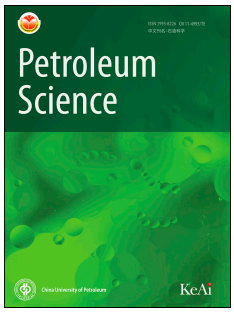

Unlocking the seal capacity of unconsolidated Quaternary hydrate-bearing sediments: carbon isotope gradients as a proxy for dynamic gas trapping efficiency

Ya-Zhou Liu, Jian-Hui Zeng, Jun-Cheng Qiao, Gui-Wen Wang, Ke-Liang Dong, Shu-Ning Liu

PII: S1995-8226(25)00488-1

DOI: https://doi.org/10.1016/j.petsci.2025.12.008

Reference: PETSCI 1348

To appear in: *Petroleum Science*

Received Date: 5 July 2025

Revised Date: 8 October 2025

Accepted Date: 4 December 2025

Please cite this article as: Liu, Y.-Z., Zeng, J.-H., Qiao, J.-C., Wang, G.-W., Dong, K.-L., Liu, S.-N., Unlocking the seal capacity of unconsolidated Quaternary hydrate-bearing sediments: carbon isotope gradients as a proxy for dynamic gas trapping efficiency, *Petroleum Science*, https://doi.org/10.1016/j.petsci.2025.12.008.

Unlocking the seal capacity of unconsolidated Quaternary hydrate-bearing sediments: carbon isotope gradients as a proxy for dynamic gas trapping efficiency

Ya-Zhou Liu[a,b,c,*], Jian-Hui Zeng[a,b,c], Jun-Cheng Qiao[a,b,c,*], Gui-Wen Wang[a,b,c], Ke-Liang Dong[a,b,c], Shu-Ning Liu[a,b,c]

[a] *State Key Laboratory of Petroleum Resources and Engineering, China University of Petroleum (Beijing), Beijing, 102249, China*

[b] *College of Geosciences, China University of Petroleum (Beijing), Beijing, 102249, China*

[c] *Hainan Institute of China University of Petroleum (Beijing), Sanya, 572025, Hainan, China*

[*] Corresponding author: maxliuyzh@163.com (Liu).

[*] Corresponding author: Juncheng.Qiao@cup.edu.cn (Qiao).

Edited by Min Li

Unlocking the seal capacity of unconsolidated Quaternary hydrate-bearing sediments: carbon isotope gradients as a proxy for dynamic gas trapping efficiency

Abstract

Submarine gas hydrate systems store vast carbon inventories (~1,500–12,400 Gt C) yet pose dual risks as potential geohazard multipliers and climate feedback agents under oceanic warming. Conventional seal assessment fails catastrophically in unconsolidated Quaternary hydrate-bearing sediments due to core-retrieval artifacts, hydrate morphology controls on capillary trapping, and meter-scale heterogeneity unresolved by seismic methods. Here, we pioneer methane carbon isotope ($\delta^{13}C_1$) gradients as a dynamic proxy for seal capacity in the Qiongdongnan Basin. Integrating petrographic features, natural gas geochemical characteristics, downhole logging data, and principal component analysis (PCA) from six wells, we: (1) quantified the thermogenic gas contribution of wells W6 and W8 to be 55%–73%, and that of well W1 to be 28%–32% via binary mixing models, (2) establish that methane carbon isotope gradients >0.5‰/m diagnose effective capillary barriers, correlating with zones of pore-throat disconnection, and (3) develop a PCA-integrated logging model (cumulative variance: 84.02%, R^2 = 0.78) predicting seal capacity from conventional petrophysical parameters. Furthermore, the results validate a charge-dynamic barrier-mixing accumulation model where thermogenic gas influx elevates hydrate saturation, creating self-sealing horizons that

trap underlying microbial gases and subsequently charged thermogenic gases, recorded in diagnostic methane carbon isotope reversals. This approach bridges molecular-scale fractionation and reservoir-scale processes, enabling targeted identification of high-integrity seals for optimized carbon storage and safer hydrate exploitation in rapidly deposited marginal basins.

Keywords: Seal capacity; Unconsolidated hydrate-bearing sediments; Carbon isotope gradients; Accumulation model; Qiongdongnan Basin

1. Introduction

The accelerating climate crisis demands innovative strategies to simultaneously mitigate atmospheric CO_2 levels and decarbonize energy systems, placing submarine gas hydrate systems at the epicenter of geoscientific urgency. These frozen methane reservoirs store ~1,500–12,400 Gt (gigatons) of carbon—surpassing global conventional gas reserves by an order of magnitude (Ruppel and Kessler, 2017; IEA, 2024)—yet their dual role as potential "geohazard multipliers" and "transitional energy sources" remains unresolved. Recent industrial breakthroughs in ultra-deepwater basins (e.g., China's Lingshui 36-1 field holding >100 Bcm gas at <500 m burial, Xu et al., 2025; India's Krishna-Godavari hydrate production test, 2024) demonstrate the technical viability of shallow-gas resourceization, aligning with IPCC's (Intergovernmental Panel on Climate Change) mandate for low-carbon fossil fuel bridging during energy transitions. Critically, however, hydrate dissociation triggered by oceanic warming (0.12 °C/decade at 500 m depth, Ruppel, 2011) could release 4–25 Gt CH_4/century—equivalent to

100–500 years of current anthropogenic emissions—amplifying climate feedback loops through abrupt methane pulses (Marín-Moreno et al., 2013, 2015; Dean et al., 2018). This existential dichotomy underscores a global imperative: developing predictive metrics to quantify dynamic seal integrity in hydrate-bearing sediments for concurrent carbon sequestration and geohazard-neutralized gas extraction.

Conventional seal assessment fails catastrophically in unconsolidated Quaternary strata, where hydrate morphology dictates pore-scale fluid trapping but evades traditional petrophysical characterization. Standard methods relying on core-derived capillary pressure (e.g., mercury injection) and permeability measurements suffer from irreducible artifacts: hydrate dissociation during retrieval alters sediment fabric (Sellm and Sloan, 1990; Feng et al., 2023; Yoshimoto et al., 2023), while drilling-induced remolding obliterates metastable grain contacts (Passchier, 2000; Zhu et al., 2021). Even advanced seismic indicators (BSRs, amplitude blanking) lack the resolution to diagnose meter-scale seal heterogeneities where >90% of slope failures initiate (Bray and Macedo, 2023; Kong et al., 2025). Compounding this, hydrate growth habit—whether pore-filling, load-bearing, or cementing—exerts first-order control on breakthrough pressure (varying by 300%–800%; Sun et al., 2022; Zhao et al., 2023), but remains invisible to well logs and basin models. Consequently, existing frameworks cannot resolve why some hydrate layers trap gigascale gas columns (e.g., Nankai Trough's 100 Bcm accumulation) while others catastrophically fail, triggering events like the Storegga Slide that released 104–504 Gt CO_2-equivalent methane (Archer, 2007; Brook

et al., 2008). This knowledge gap represents a fundamental Earth system process blind spot, impeding both IPCC's "Blue Carbon" sequestration agenda and UNISDR's (United Nations Office for Disaster Risk Reduction) geohazard mitigation goals.

Here, we pioneer methane carbon isotope gradients as a geochemical proxy for dynamic seal capacity. Integrating downhole logging, geochemical profiling and analytical data, and principal component analysis (PCA), we establish a quantitative framework that: (1) deciphers thermogenic vs. biogenic methane contributions in mixed-source systems, (2) correlates isotopic discontinuities with capillary barrier strength, and (3) resolves transient gas trapping in hydrate-bearing sequences. Using the Qiongdongnan Basin as a natural laboratory, we demonstrate that peak gradients >0.5‰/m diagnose effective seals where traditional petrophysics fails. Our approach bridges molecular-scale fractionation processes and basin-scale carbon budgets, ultimately enabling predictive mapping of seal integrity for optimized carbon storage and safer gas hydrate exploitation.

2. Geological setting

The Qiongdongnan Basin (QDNB) is a Cenozoic rift basin on the continental margin of the northern South China Sea (Fig. 1(a)), with an area of approximately 8.3×10^4 km^2 (Cao et al., 2022; Liu et al., 2023). The QDNB is adjacent to the Hainan Uplift in the north, and the Xisha Uplift in the south, and is sandwiched between the Pearl River Mouth Basin (PRMB) and the Yinggehai Basin (YGHB) in the east and west (Fig. 1(c)). It is an important deep-water (water depth greater than 1000 m) hydrocarbon

resource exploration area in the northern part of the South China Sea (Xu et al., 2025; Zhang et al., 2025). From north to south, it can be further divided into four tectonic units: the northern depression zone (Songtao and Yacheng Sags), the central uplift zone (Songtao, Lingshui and Yacheng Uplifts), the central depression zone (Songnan, Lingshui, Ledong, Changchang, Baodao, and Beijiao Sags) and the southern uplift zone (Cao et al., 2022). Since the Paleocene, the QDNB has experienced syn-rifting and post-rifting periods due to the interaction between the Pacific Plate and the Eurasian Plate and the seafloor spreading in the South China Sea, bounded by the regional unconformity T60 (23 Ma) (Fig. 1(b)) (Zhang et al., 2021).

Fig. 1. (a) Modern surface elevation map showing the location of the Qiongdongnan Basin (QDNB), Yinggehai Basin (YGHB) and Pearl River Mouth Basin (PRMB) in the South China Sea. **(b)** Comprehensive stratigraphic column diagram of the Qiongdongnan Basin (Lai et al., 2024). **(c)** Regional location and structural divisions of the Qiongdongnan Basin.

Supplied by sediments from Hainan Island, Vietnam, and the Red River system, the sediment-fill sequence of the QDNB contains up to 8 km of clastic sediments ranging in age from the Paleogene to the Quaternary (Su et al., 2023). Coal in the Oligocene Lingshui and Yacheng Formations is the main gas-prone source rock (Fig. 1(b)) (Xiao et al., 2006). The sandstone units deposited in the Lingshui, Sanya, and

Huangliu Formations are potential reservoirs. The thick mudstones of the Late Miocene Huangliu Formation and the Pliocene Yinggehai Formation provide an excellent regional seal for hydrocarbon accumulation. The Quaternary Ledong Formation is dominated by regional mudstone deposits, with sandy gravity flow deposits locally developed in the slope-folding area and submarine plains, and it is the main target for the exploration of ultra-deepwater and ultra-shallow layers in the basin (water depth over 1500 m, and burial depth below the seafloor less than 500 m).

3. Samples and methods

3.1. Sample collection

A total of 14 natural gas samples were collected from 6 wells in the Quaternary Ledong Formation of the QDNB, which were analyzed for natural gas components and carbon isotopes. The locations of the gas sample collection wells are shown in Fig. 1(c). Although only 14 new gas samples were analyzed, these were compared with 33 previously published datasets, and the main interpretations are supported by continuous isotope logging data (~200 points per well across six wells), which together provide sufficient statistical robustness and regional representativeness. Natural gas samples analyzed in this study were obtained through Modular Formation Dynamics Tester (MDT) and Drill Stem Test (DST) operations during drilling. Both methods allow direct sampling of formation fluids at near in-situ pressure and temperature conditions, which effectively minimizes post-recovery alteration of the gas composition. The collected gas was immediately transferred into high-pressure stainless-steel cylinders for storage and

126 transportation, ensuring that the samples remained stable before geochemical analysis.

127 During MDT sampling, a probe was set against the borehole wall to establish
128 hydraulic communication with the formation, followed by controlled drawdown to
129 extract free gas or dissolved gas released from formation fluids. The sampling was
130 performed under downhole pressure conditions, preventing hydrate dissociation during
131 the process. Similarly, in DST operations, formation gas flowed through the drill stem
132 under controlled bottom-hole pressure, and representative gas samples were taken in
133 sealed cylinders. These procedures ensured that the gas collected reflected the in-situ
134 free gas phase of the reservoir rather than secondary gases released during core recovery
135 or hydrate dissociation.

136 A key concern in gas sampling is the potential migration of pore gas along the
137 borehole, which could lead to cross-contamination between different depth intervals. To
138 mitigate this, both MDT and DST employed packers and flow isolation systems to
139 hydraulically seal off the target interval during sampling. This design prevented vertical
140 gas flow within the borehole and ensured that the collected gas was solely derived from
141 the specified formation horizon.

142 *3.2. Natural gas component and carbon isotope analysis*

143 Natural gas components and carbon isotopes were measured at the National Key
144 Laboratory of Petroleum Resources and Engineering, China University of Petroleum
145 (Beijing). Natural gas components were analyzed using an Agilent 8890 gas
146 chromatograph (GC) equipped with a flame ionization detector. A capillary column

147 (PLOT Al_2O_3, 27 m × 0.32 mm × 0.25 μm) was used for the separation of individual
148 hydrocarbon gas components from methane to *n*-heptane (C_1–C_8). The initial
149 temperature of the column oven was set at 60 °C and maintained for 1 min. The
150 temperature was then increased to 80 °C at a rate of 20 °C/min, and then to 190 °C at a
151 rate of 30 °C/min for 7 min. Helium was used as the carrier gas at a constant flow rate
152 of 1.0 mL/min.

153 Carbon isotope analysis was performed using the Trace GC-ISOLINK-MAT 253
154 IRMS test system. A silica capillary column (HP-PLOT Q 30 m × 0.53 mm × 40 μm)
155 was used to separate the individual alkane gases (C_1–C_5) and carbon dioxide (CO_2). The
156 initial temperature of the chromatogram was 40 ℃ with a constant temperature of 6 min,
157 and the temperature was increased to 80 ℃ at 15 ℃/min, and then to 200 ℃ at
158 5 ℃/min with a constant temperature of 5 min. The results were based on the Vienna
159 Pee Dee Belemnite standard ($\delta^{13}C_{VPDB}$ = 0‰) as a reference. Each sample was analyzed
160 three times and the average value was taken with an analytical precision of ±0.5‰.

161 *3.3. Well logs*

162 We employed logging-while-drilling (LWD) data from the six wells mentioned
163 above to interpret lithology and fluid properties. A standard suite of logging curves,
164 including gamma ray, sonic, density, neutron, and resistivity, have been used to infer a
165 range of reservoir properties such as porosity, gas saturation, and hydrate saturation.
166 These log curves have been corrected for hole size, casing size and drilling fluid type
167 before being interpreted and processed.

3.4. Temperature and pressure measurements

In-situ temperature and pressure profiles were acquired using Schlumberger's Modular Formation Dynamics Tester (MDT) with a Quicksilver Probe module. The measurement principle involves deploying a dual-packer probe to hydraulically isolate the target formation, followed by controlled fluid withdrawal to induce transient pressure-temperature responses. Formation pressures were measured via dual quartz crystal gauges (±0.01 psi accuracy), while temperatures were recorded using platinum RTD sensors (±0.05 °C accuracy), both calibrated against NIST-traceable standards. Depth positioning was validated through gamma-ray log correlation (<0.15 m vertical uncertainty). Pressure data were calibrated against downhole mud weight gradients, revealing a 0.03 (±0.005) psi offset corrected for near-wellbore supercharging, while temperature measurements incorporated transient heat transfer corrections validated against distributed temperature sensing (DTS) baselines. The in-situ temperatures and pressures are subsequently combined with natural gas components and pore water salinity to estimate hydrate phase boundaries (Tishchenko et al., 2005; Riedel et al., 2021).

3.5. Carbon isotope gradient calculation

Continuous methane $\delta^{13}C_1$ profiles (mud gas isotope logging) from six Quaternary hydrate-bearing boreholes were analyzed to quantify vertical isotopic gradients (G), representing the first derivative of carbon isotope composition with respect to depth (Fig. 2(a)). Raw $\delta^{13}C_1$ data were smoothed using a Savitzky-Golay filter to suppress

high-frequency noise while preserving trends linked to gas migration. The instantaneous gradient at any depth position z is defined as:

$$G(z) = \frac{\mathrm{d}\delta^{13}\mathrm{C}_1(z)}{\mathrm{d}z} = \lim_{\Delta z \to 0} \frac{\delta^{13}\mathrm{C}_1(z+\Delta z) - \delta^{13}\mathrm{C}_1(z)}{\Delta z} \quad (1)$$

where z is the vertical depth, m; $\delta^{13}C_1$ is the methane carbon isotope composition at depth z, ‰; $G(z)$ is the vertical methane carbon isotope gradient, ‰/m. This differential approach captures the tangent slope of $\delta^{13}C_1$ variations across lithological boundaries, providing critical insights into gas migration mechanisms. The gradient spectrum reveals two end-member scenarios: (1) $G \to 0$ indicates isotopic homogenization through diffusion-dominated migration, reflecting ineffective capillary sealing and continuous gas leakage (Fig. 2(b)); (2) $G \to \infty$ corresponds to sharp isotopic discontinuities diagnostic of intact capillary seals, where abrupt $\delta^{13}C_1$ shifts mark arrested gas migration and efficient hydrocarbon accumulation.

Fig. 2. (a) Vertical methane $\delta^{13}C_1$ profile and isotopic gradients. **(b)** Conceptual models linking isotopic gradients to gas trapping efficiency.

3.6. Principal component analysis

Principal component analysis (PCA) is a multivariate statistical technique that reduces high-dimensional data into orthogonal components while retaining critical information on variance and covariance structures (Jolliffe and Cadima, 2016). Here,

PCA was applied to integrate methane carbon isotope gradients and multi-logging parameters for constructing a composite petrophysical-geochemical proxy. The raw dataset was preprocessed in OriginPro 2023, where all input variables were normalized using the min–max method to a uniform scale of [0, 1], thereby eliminating scale disparities, and outliers beyond three standard deviations (>3σ) were iteratively removed through Mahalanobis distance filtering. PCA was performed using Origin's built-in multivariate analysis module, which decomposes the covariance matrix via singular value decomposition (SVD) to extract principal components (PCs) (Wold et al., 1987; Abdi and Williams, 2010). Those principal components that retained the ability to explain greater than 80% of the cumulative variance were selected as the integrated logging score, with variable loadings revealing strong correlations between $\delta^{13}C_1$ and logging. Multiple linear regression models were established in Origin, validated by leave-one-out cross-validation, linking the logging-derived score to isotopic signatures. This approach bridges geochemical fingerprints and geophysical logging responses, offering a robust tool for evaluating methane migration and seal capacity.

4. Results

4.1. Petrographic features

The detailed petrography shows that the Quaternary Ledong Formation sediments are composed of skeletal and non-skeletal components, with specific loose-unconsolidated characteristics between them (Fig. 3(a) and (c)). The detrital fraction is dominated by quartz (65%–85% of non-skeletal components), with

subordinate feldspar (5%–20%), lithic fragments (5%–20%), and clay minerals (Fig. 3(b), (e)–(i)). Quartz grains display angular to subangular morphologies, suggesting proximal transport. Biogenic constituents are characterized by well-preserved planktonic foraminifera alongside fragmented bioclasts exhibiting varying degrees of mechanical abrasion (Fig. 3(e)–(i)). The bioclast size spectrum mainly ranges from 50 to 500 μm. Sedimentologically, the formation consists of alternating sandy and muddy sediments. Sandy intervals are predominantly fine- to medium-grained with occasional coarse grains. Grain size analysis reveals moderate to poor sorting. Grain relationships predominantly show floating or point contacts (90%–95% of grain contacts) with minimal compaction-induced deformation. Post-depositional features include hydrate dissociation structures observed in core samples after 72-hour atmospheric exposure. These manifest as mm-scale vugular pores with delicate ice-lattice pseudomorphs along pore margins (Fig. 3(d)), suggesting in situ methane hydrate destabilization during core retrieval.

Fig. 3. The photographs showing the different petrographic and mineralogical features observed in the Ledong Formation. **(a)** Well W1, 1826.0 m, fine-grained sandy sediments, washed cuttings; **(b)** Well W1, 1896.0 m, fine-grained sandy sediments, floating or point contacts; **(c)** Well W1, 1902.0 m, loose plug sample, fine-medium grains visible; **(d)** Well W4, 1871.03-1871.47 m, pores remaining after hydrate decomposition; **(e)** Well W4, 1866.5 m, bioclastic debris. **(f)** Well W4, 1871.1 m,

fine-grained sandy sediments, floating or point contacts; **(g–i)** Well W6 samples (1766.1 m, 1766.5 m and 1768.7 m) display analogous fine-grained sandy sediments, floating or point contacts between grains. Q: quartz; D: lithic debris; B: bioclasts; F: feldspar.

4.2. Geochemical characteristics of natural gas

The composition of natural gases in the study area, dominated by hydrocarbon gases with methane (C_1) contents ranging from 95.7% to 99.6% (mean: 98.2%), exhibits a pronounced dry gas signature (Table 1). This is evidenced by low C_{2+} heavy hydrocarbon content (ethane and propane: 0.02%–0.81%, mean: 0.35%) and high dryness coefficients (C_1/C_{1-5}: 0.98–0.99, mean: 0.99). These compositional characteristics reflect influences from source rock organic matter type, thermal maturity, and potential migration processes.

Table 1. Chemical and isotopic compositions of hydrate-related gases, gases in this study area, and deep gases in the QDNB.

Well	Formation	Meter below seafloor (mbsf), m	Natural gas components, %		C_1/C_{2-3}	C_1/C_{1-5}	Carbon isotope composition		References
			C_1	C_2+C_3			$\delta^{13}C_1$, ‰	$\delta^{13}C_2$, ‰	
GMGS5-W08	Ledong	8.0	97.69	2.1	46.5	0.98	−59.5	−26.0	Lai et al. (2021)
		62.9	81.21	17.46	4.7	0.86	−56.3	−26.9	

		148.4	79.16	19.55	4.0	0.85	−50.4	−26.5	
QDNB-08B-2018	Ledong	17.0	97.50	2.0	48.8	0.98	−56.9	−26.6	Wei et al. (2021)
		27.0	90.70	8.5	10.7	0.91	−58.2	−27.2	
		32.7	91.70	7.5	12.2	0.92	−58.8	−28.1	
		60.0	95.60	4.1	23.3	0.96	−62.5	−28.4	
		62.9	85.70	12.8	6.7	0.86	−59.7	−28.4	
		63.7	84.50	14.0	6.0	0.85	−57.2	−27.9	
		63.7	96.70	3.1	31.2	0.97	−63.7	−28.8	
		63.9	89.00	10.0	8.9	0.89	−57.6	−27.9	
		64.5	87.70	11.0	8.0	0.88	−60.0	−29.0	
		64.7	97.20	2.7	36.0	0.97	−61.1	−29.2	
		69.3	88.00	10.6	8.3	0.88	−62.8	−28.7	
		170.2	72.50	23.4	3.1	0.73	−52.0	−27.0	
LS1728	Huangliu	3305.2	89.56	/	/	0.92	−40.2	−25.9	Zhu et al. (2021)
		3406.5	90.82	/	/	0.92	−38.9	−26.0	
LS1724	Huangliu	3251.0	90.23	/	/	0.92	−39.1	−25.4	
		3251.0	90.55	/	/	0.92	−39.0	−25.4	

		3355.0	92.90	/	/	0.98	−39.2	−25.5	
		3445.0	90.64	/	/	0.92	−38.4	−25.8	
SS1721	Huangliu	3306.0	92.51	/	/	0.94	−36.8	−23.5	Huang et al. (2016)
		3324.0	93.25	/	/	0.94	−36.8	−23.6	
		3366.4	92.69	/	/	0.94	−37.3	−23.8	
		3368.5	92.56	/	/	0.94	−36.8	−24.1	
		3321–3351	92.99	/	/	0.94	−37.3	−24.1	
SS1723	Huangliu	3407.0	89.45	/	/	0.93	−37.8	−25.3	
SS1722	Huangliu	3228.5	91.68	/	/	0.94	−38.2	−23.8	
	Huangliu	3331.3	93.04	/	/	0.93	−37.4	−24.2	
SS2211	Huangliu	3339.0	91.12	/	/	0.92	−39.4	−26.2	
		3391.0	91.53	/	/	0.93	−39.2	−26.2	
		3352.5	91.37	/	/	0.93	−38.8	−26.0	
W1	Ledong	263.6–273.2	98.0	0.08	1294.8	0.99	−52.8	−19.6	This study
		263.6–273.2	99.5	0.10	1014.9	0.99	−53.0	−19.7	
		263.6–273.2	98.4	0.12	843.7	0.99	−52.2	−20.0	
W6	Ledong	215.6–225.4	97.7	0.20	485.0	0.99	−47.2	−20.5	

		215.6–225.4	95.7	0.67	142.0	0.99	−46.8	−20.6
		215.6–225.4	97.8	0.40	244.2	0.98	−46.5	−20.3
		230.4–240.5	99.6	0.02	4980.0	0.99	−47.2	−20.9
		230.4–240.5	98.6	0.05	2086.0	0.98	−47.0	−21.0
		230.4–240.5	96.8	0.04	2518.3	0.99	−47.3	−20.6
W8	Ledong	217.1–230.2	98.56	0.43	229.2	0.99	−45.3	−21.1
		217.1–230.2	98.12	0.59	166.3	0.98	−46.9	−23.6
		217.1–230.2	98.37	0.60	164.0	0.98	−45.4	−24.7
		217.1–230.2	98.86	0.81	122.0	0.99	−43.8	−19.7
		217.1–230.2	98.97	0.73	135.6	0.99	−46.7	−20.6

Note: /, no data.

Carbon isotopic compositions ($\delta^{13}C_1$ and $\delta^{13}C_2$) provide critical insights into gas origins and source rock affinities (Dai et al., 2005; Xiao et al., 2006; Milkov et al., 2018). The $\delta^{13}C_2$ values in the study area range from −24.7‰ to −19.6‰ (mean: −20.9‰), consistent with coal-type thermogenic gases derived from humic organic matter (Table 1 and Fig. 4(a)). However, cross-plots of $\delta^{13}C_1$ versus $\delta^{13}C_2$ and $\delta^{13}C_1$ versus C_1/C_{2-3} reveal a predominance of mixed gas origins (Fig. 4(b)). Specifically, $\delta^{13}C_1$ values (−53.0‰ to −43.8‰) intermediate between deep Huangliu thermogenic gases ($\delta^{13}C_1$: −40.2‰ to −36.8‰) and ultra-shallow microbial hydrate gases ($\delta^{13}C_1$:

276 <−55‰) suggest contributions from both thermogenic and microbial sources (Fig. 4(a)).
277 Notably, well W1 exhibits microbial gas characteristics, suggesting a higher proportion
278 of microbial input relative to thermogenic gas (Fig. 4(b)).
279
280 **Fig. 4.** Genetic diagrams of $\delta^{13}C_1$ versus $\delta^{13}C_2$ **(a)** and $\delta^{13}C_1$ versus C_1/C_{2-3} **(b)** for
281 various gases in the QDNB. The geochemical data of deep gases and hydrate-related
282 gases have been cited in previous studies. See Table 1 for details.
283
284 The thermogenic component primarily originates from Yacheng Formation
285 coal-measure source rocks, which are widely distributed in the QDNB's deep-water
286 regions. These source rocks, characterized by high TOC contents and thermal maturities,
287 have generated substantial coal-type gases that migrated vertically or laterally into
288 shallow reservoirs (Su et al., 2012; Ren et al., 2022; Pei et al., 2024). Microbial activity,
289 typically active at 35–75 °C (Rice and Claypool, 1981; Scott et al., 1994; Stolper et al.,
290 2014), is theoretically constrained to 800–1825 m burial depths under local geothermal
291 conditions (40 °C/km) in the QDNB (Yuan et al., 2009; Zhang et al., 2014). However,
292 the Ledong reservoirs' current burial depths fall outside this microbial window,
293 suggesting limited in situ microbial gas generation. Instead, microbial contributions
294 likely derive from biodegradation of pre-existing thermogenic gases or mixing with
295 deeper microbial gases generated in Huangliu-Meishan strata, despite their low TOC
296 contents (Ye et al., 2019; Lai et al., 2022). This multi-source charging system highlights

297 the complexity of gas accumulation processes in ultra-deepwater, ultra-shallow
298 reservoirs.

299 *4.3. Characteristics of the natural gas hydrate stability zone*

300 Integration of in-situ temperature measurements with core-derived pore water
301 salinity values and gas compositional analyses enables precise determination of the
302 methane hydrate phase boundary at the study sites (Fig. 5). At all investigated locations,
303 pore water salinities remain near 35 PSU (Practical Salinity Unit), consistent with
304 normal marine conditions. Seafloor depths across the study area range from 1513.35 to
305 1616.00 m, with thermal gradients derived from multiple tool deployments showing
306 considerable spatial variation between 42.7 and 56.3 °C/km. These parameters intersect
307 the phase stability boundary for methane hydrate (35 PSU salinity) at depths of 247–347
308 mbsf (Fig. 5(a)–(f)). At Site W8, while no direct temperature measurements are
309 available, pore water salinity data exhibit comparable characteristics to adjacent sites.
310 We therefore employ the well-constrained geothermal gradient from Site W13
311 (49.2 °C/km) to model the base of the gas hydrate stability zone (BGHSZ) at this
312 location (Fig. 5(e)). Our analysis reveals two key relationships: (1) BGHSZ depth
313 increases systematically with seafloor depth, and (2) higher thermal gradients reduce
314 BGHSZ depth.

315

316 **Fig. 5.** Calculation of the depth of the base of the gas hydrate stability zone (BGHSZ) at
317 different sites. **(a)** well W1; **(b)** well W3; **(c)** well W4; **(d)** well W6; **(e)** well W8; **(f)**

318 well W13.

319

320 Drilling observations and well-log evaluations demonstrate widespread but
321 heterogeneous hydrate occurrence across the study area. Hydrate-bearing intervals are
322 identified at 6 of 7 sites, with the exception of Site W1 where no significant
323 accumulations were detected. Measured hydrate layers range from 2.3 to 4.7 m thick
324 (mean 3.6 m), substantially thinner than the 247–347 m theoretical stability zone
325 thickness predicted by phase equilibrium modeling. This discrepancy likely reflects
326 multiple controlling factors: (a) Low-permeability fine-grained sediments (e.g.,
327 clay-rich deposits) act as effective fluid barriers, restricting vertical diffusion fluxes of
328 free gas (Bourg et al., 2017; Neuzil, 2019; Hu et al., 2024). This sedimentary
329 architecture promotes preferential hydrate enrichment at chimney tops. (2) Sustained
330 hydrate growth requires prolonged geologic timescales to maintain stable
331 thermal-pressure conditions and continuous gas fluxes (Fisher, 2005; Joye et al., 2005;
332 Kasala et al., 2024). The short sedimentation time of the Ledong Formation in the study
333 area (<0.8 Myr) resulted in the failure to reach phase equilibrium conditions, thus
334 inhibiting the large-scale accumulation of hydrates. (3) Late Quaternary seismic activity
335 (Lüdmann et al., 2001; Shi et al., 2017; Ye et al., 2018) and regional uplift have
336 triggered reorganization of the pressure regime. Such tectonic perturbations not only
337 induce in situ dissociation of preexisting hydrates but also facilitate secondary
338 redistribution through newly generated fluid escape pathways, resulting in dynamic

evolution of "non-steady-state" reservoir configurations. These findings align with global statistical patterns of passive margin hydrate systems. Although the base of the gas hydrate stability zone (GHSZ) can be estimated thermodynamically, numerous studies have shown that the actual thickness of gas hydrate accumulations is often significantly smaller than the theoretical stability zone (Klauda and Sandler, 2005; Boswell and Collett, 2011; Ruppel, 2011).

4.4. Methane carbon isotope profile

Systematic variations in methane isotopic composition are observed both vertically and laterally across the study area. The most ^{13}C-depleted methane values (mean $\delta^{13}C_1$ = −53.4‰) are recorded at well W1, while free methane collected from well W4 exhibits the most enriched carbon isotopic signature (mean $\delta^{13}C_1$ = −42.5‰) (Fig. 6). Spatial analysis reveals a systematic northeastward enrichment in methane $\delta^{13}C$ values (−53.4‰ to −42.5‰) along the structural trend. A plot of C_1/C_{2+3} ratios and $\delta^{13}C_1$ values (Fig. 4(b)), combined with $\delta^{13}C_2$ values (Fig. 4(a)), indicates mixing of thermogenic and biogenic methane sources.

Fig. 6. Methane carbon isotope profiles at different sites. **(a)** well W1; **(b)** well W8; **(c)** well W13; **(d)** well W6; **(e)** well W3; **(f)** well W4.

The systematic $\delta^{13}C_1$ oscillations (−70‰→−50‰→−70‰) that we highlight in this study are most clearly observed in well W6 (Fig. 6). This well is unique in that

continuous downhole isotope logging was obtained across a sufficiently thick interval, thereby recording the complete migration–trapping–remobilization cycle. In contrast, the isotopic datasets from wells W8, W13, W3, and W4 primarily capture thermogenic gas charging and the development of effective top-seals, whereas well W1 mainly reflects thermogenic gas input without subsequent remobilization. The limited depth penetration of most wells (typically ~200–300 m below seafloor) further constrains the vertical coverage of isotope measurements and precludes documentation of the full oscillatory pattern.

Nevertheless, despite these differences in data completeness, the combined isotopic profiles from all wells provide a consistent picture. Taken together, they delineate the critical processes of thermogenic gas input, microbial mediation, and seal formation within a broadly similar depositional–structural framework across the study area. Thus, while well W6 uniquely records the full tripartite $\delta^{13}C_1$ signature, the complementary evidence from other sites reinforces the interpretation that this isotopic oscillation reflects a fundamental, regionally significant cycle of subsurface carbon migration and recycling.

5. Discussion

5.1. Estimation of the proportion of natural gas sources

Natural gas mixing is typically regarded as a physical process wherein chemical composition remains conserved (Schoell, 1983; Snowdon, 2001; Chen et al., 2025). Governed by the principle of mass balance, the stable isotopic composition (e.g., $\delta^{13}C$)

of individual components within a mixed-source reservoir is predominantly controlled by their respective isotopic signatures in the contributing end-member gases and the proportions in which they mix. The resultant isotopic value ($\delta^{13}C_{i,M}$) of a specific component "*i*" (e.g., CH_4, C_2H_6) in the mixture (M) can be expressed as a concentration-weighted average (Eq. (2)):

$$\delta^{13}C_{i,M} = \frac{\alpha \times N_{i,A} \times \delta^{13}C_{i,A} + (1-\alpha) \times N_{i,B} \times \delta^{13}C_{i,B}}{\alpha \times N_{i,A} + (1-\alpha) \times N_{i,B}} \quad (2)$$

where *A* and *B* represent the two distinct end-member gases. *i* denotes a specific molecular component (e.g., CH_4, C_2H_6). α is the fractional contribution of end-member A ($0 \leq \alpha \leq 1$), and $(1-\alpha)$ is the contribution of end-member B. $N_{i,A}$ and $N_{i,B}$ are the mole fractions (in %) of component "*i*" in end-member gases A and B, respectively. $\delta^{13}C_{i,A}$ and $\delta^{13}C_{i,B}$ are the carbon isotopic compositions (in ‰ VPDB) of component "*i*" in end-member gases A and B, respectively.

This theoretical model provides a viable alternative to complex experimental simulations for quantitatively estimating mixing proportions (α) when the end-member gases exhibit distinct isotopic signatures and possess comparable thermal maturities. However, inherent non-uniqueness (multi-solution potential) exists when applying this model. Different parameter choices (e.g., selecting $\delta^{13}C_1$ vs. $\delta^{13}C_2$) can yield disparate mixing ratios. Consequently, careful consideration of parameter applicability within the specific geological context is paramount. Existing research demonstrates that methane carbon isotopes ($\delta^{13}C_1$) are highly sensitive to thermal maturation effects, making them

suitable for discerning mixtures of gases sharing a common source but differing in maturity (Chung and Sackett, 1979; Liu et al., 2019). In contrast, ethane carbon isotopes ($\delta^{13}C_2$) exhibit a stronger inheritance from the original organic precursor, rendering them more effective for quantifying the proportions of mixed gases derived from distinct source types (e.g., terrigenous vs. marine organic matter), particularly when their maturities are similar (Berner and Faber, 1988; Liu et al., 2019).

Integrated analysis of the geological setting, natural gas composition, and carbon isotopic evidence within the Ledong Formation study area reveals a dual-source hydrocarbon charging model dominated by deep thermogenic gas and shallow biogenic gas (Fig. 4). Application of the binary mixing model (Eq. (2)) requires initial characterization of the composition (specifically methane content, C_1) and methane carbon isotopic ratio ($\delta^{13}C_1$) for end-member gases derived solely from each source. Utilizing published data and our own measurements (Table 1), two representative end-member gas samples are selected: a deep gas sample (representative of the Yacheng Formation source rock) and a shallow hydrate-related gas sample (representative of the intra-Ledong Formation source rock). Consequently, the methane content and $\delta^{13}C_1$ values (expressed as averages; Table 2) from these end-members serve as input parameters for the mixing model, enabling quantification of the relative contributions from each source to mixed gases. Finally, based on the $\delta^{13}C_1$ values, an interpretive chart is constructed to estimate mixing proportions within the study area (Fig. 7).

Table 2. Composition and carbon isotope characteristics of end-member gases (data from Table 1).

End-member gases	CH_4, %	$C_1/C_{1\text{-}5}$	$\delta^{13}C_1$, ‰	$\delta^{13}C_2$, ‰
Deep gas samples (representative of the Yacheng Formation source rock)	91.58	0.93	−38.3	−25.0
Hydrate related gas samples (representative of the intra-Ledong Formation source rock)	91.01	0.92	−58.7	−27.2

Fig. 7. Carbon isotope characteristics of methane in gases from different source mixtures and analysis of mixed-source ratios.

Utilizing the interpretive chart derived from methane carbon isotope values ($\delta^{13}C_1$; Fig. 7), the relative contributions of deep thermogenic gas and shallow biogenic gas to individual reservoirs within the Ledong Formation are quantified. Well W1 gas is predominantly sourced from shallow biogenic gas (68%–72% contribution), while gases from wells W6 and W8 are primarily derived from deep thermogenic sources (55%–73% contribution). It is important to acknowledge the inherent complexity of natural gas mixing. Secondary processes, including isotopic fractionation effects during migration and accumulation, can influence the $\delta^{13}C_1$ values measured in the reservoir (Barker and Fritz, 1981; Zhang et al., 2001; Xia et al., 2012). Our application of the binary mixing model did not explicitly account for these potential fractionation effects, which may

introduce some uncertainty into the estimated contribution percentages. Despite this limitation, the calculated mixing proportions are broadly consistent with the established geological framework of the study area. This approach provides a valuable quantitative assessment of the relative contributions from distinct sources within the mixed gas accumulations of the Ledong Formation.

5.2. Quantitative evaluation of sealing capacity

Direct in situ measurement of key sealing capacity parameters—such as capillary entry pressure and permeability—in unconsolidated Quaternary sediments containing gas hydrates poses significant challenges. Furthermore, the complex hydrate growth modes (e.g., cementing, pore-filling, load-bearing) inherent to different reservoir types exert a primary control on pore structure (Waite et al., 2009; Mahabadi et al., 2019), further complicating traditional assessment methods. Critically, the depth gradient of methane carbon isotope ratios ($\delta^{13}C_1$) provides an integrated proxy for sediment sealing capacity, reflecting processes governed by isotopic fractionation during gas migration and retention. To leverage this relationship, we developed a novel quantitative model for sealing capacity evaluation, as demonstrated using well data from the study area (Fig. 8). Firstly, a continuous depth profile of methane $\delta^{13}C_1$ values is constructed from downhole logging measurements. Secondly, the isotopic logging data are smoothed using a Savitzky–Golay filter with a window size of 20 data points and a second-order polynomial, parameters chosen to minimize noise while preserving the primary oscillation features. Thirdly, the first derivative of the smoothed $\delta^{13}C_1$ profile is

460 computed to determine the methane carbon isotope gradient at each depth. Finally,
461 multiple conventional well-log responses (e.g., resistivity, acoustic velocity, density) are
462 integrated using Principal Component Analysis (PCA). This dimensionality reduction
463 technique yields principal component scores and a composite log signature score. A
464 quantitative model for predicting the sealing capacity of unconsolidated,
465 hydrate-bearing sediments is established by calibrating the relationship between the
466 composite log signature score and the methane carbon isotope gradient.
467
468 **Fig. 8.** The procedure of establishing a quantitative evaluation model for sediment
469 sealing capacity based on the methane carbon isotope gradient.
470
471 Based on the pre-established gas hydrate stability zone modeling, the study area
472 exhibits potential for hydrate accumulations of variable thickness. Diagnostic well-log
473 responses confirm natural gas hydrate presence through: (1) significantly reduced
474 acoustic transit time (DT), (2) markedly elevated compressional (V_p) and shear wave (V_s)
475 velocities, (3) sharply increased true formation resistivity (RT), (4) slightly decreased
476 bulk density (DEN), (5) low natural gamma ray (GR) values, and (6) a pronounced
477 reduction in V_p/V_s ratio (Moridis et al., 2011; Collett and Lee, 2012; McConnell et al.,
478 2012). Integrated analysis of these diagnostic signatures identifies a 4.75 m-thick gas
479 hydrate interval in well W4 between 1866.00–1870.75 m (Fig. 9). The methane carbon
480 isotope gradient peaks at ~1866 m and decreases systematically toward shallower and

deeper strata (Fig. 9). This gradient pattern provides indicative evidence of isotopic disequilibrium across adjacent formations, demonstrating effective sediment sealing at this horizon. Furthermore, the downward decline in the methane carbon isotope gradient reveals that the hydrate layer functions as a heterogeneous seal with maximum sealing capacity at its top, progressively weakening downward. This heterogeneity likely reflects controls by hydrate growth modes (e.g., transition from pore-filling to cementing habit) on pore architecture and capillary seal capacity.

Fig. 9. Logging curves from the W4 drilling site, located at a water depth of 1616.00 m. MD: Measured depth; GR: Natural gamma ray logging; CAL: Caliper logging; DT: Acoustic transit time logging; DEN: bulk density logging; RT: True formation resistivity logging; V_p: Compressional wave velocity logging; V_s: Shear wave velocity logging; Sg: Gas saturation.

Conventional well-log attributes exhibit strong non-uniqueness in subsurface interpretation due to coupled influences from lithology, physical properties, and hydrocarbon saturation. To establish a robust quantitative linkage between standard logging responses and methane carbon isotope gradient variations, we developed an enhanced multi-attribute predictive framework. This framework integrates not only seven key petrophysical parameters—Gamma Ray (GR), Acoustic Transit Time (DT), Bulk Density (DEN), True Formation Resistivity (RT), Compressional Wave Velocity

(V_p), Shear Wave Velocity (V_s), and V_p/V_s ratio—but also incorporates their depth-derived gradients (slopes). By transforming all input variables into "rate-of-change" or "gradient" indicators, this approach captures instantaneous responses of different physical properties to the same underlying geological processes, thereby reducing interpretive ambiguity.

Given the significant disparities in measurement units and value ranges among the original parameters and their gradients, direct comparability for Principal Component Analysis (PCA) is precluded. We therefore implemented max-min normalization to standardize all input variables to a uniform [0, 1] scale:

$$X_{i,\mathrm{norm}} = \frac{X_i - X_{i,\mathrm{min}}}{X_{i,\mathrm{max}} - X_{i,\mathrm{min}}} \tag{3}$$

where $X_{i,\mathrm{norm}}$ is the normalized value, X_i is the original measurement (either the raw log value or its depth gradient), and $X_{i,\mathrm{min}}$, $X_{i,\mathrm{max}}$ are the parameter-specific minimum and maximum values across the study interval, respectively. This linear transformation preserves intrinsic data relationships while enabling dimensionally homogeneous feature integration essential for PCA-driven dimensionality reduction.

Following standardization of the 14 resulting variables (7 original parameters + 7 gradient parameters), PCA is performed with cumulative variance explained >85%. The principal component analysis extracted five significant components with eigenvalues greater than 0.7, together explaining 84.02% of the total variance (Table 3). PC1 has the highest eigenvalue (3.10) and accounts for 22.17% of the variance, with strong positive loadings on V_s, V_p, and RT (Table 4). This component integrates acoustic–resistivity

attributes and primarily reflects hydrate saturation and pore fluid effects. PC2 explains 21.64% of the variance, dominated by DT, V_p/V_s ratio, and velocity-related slopes (V_p and V_s), indicating elastic property variations and compaction-related lithological controls. PC3 contributes 18.45% of the variance, with high negative loadings on GR, DEN, and V_p/V_s, highlighting clay content and density heterogeneity that affect reservoir quality and hydrate occurrence. PC4, accounting for 16.57% of the variance, is mainly governed by GR, DEN, and V_p/V_s slope parameters, reflecting vertical heterogeneity and seal capacity within hydrate-bearing intervals. PC5, with a smaller contribution of 5.19%, captures higher-order variations through GR, DEN, and RT slopes, which likely represent fine-scale lithological changes and diagenetic effects. Together, these components demonstrate that PC1 and PC2 capture the dominant hydrate-related acoustic–resistivity and lithological controls, whereas PC3–PC5 represent secondary influences from mineral composition, vertical heterogeneity, and localized diagenesis.

Table 3. Percentage of variance explained by PCA and eigenvalues of each component.

Principal component number	Eigenvalue	Percentage of variance explained, %	Cumulative percentage of variance explained, %
1	3.10	22.17	22.17
2	3.03	21.64	43.82
3	2.58	18.45	62.26
4	2.32	16.57	78.83
5	0.73	5.19	84.02
6	0.64	4.56	88.58

7	0.59	4.24	92.82
8	0.44	3.11	95.93
9	0.28	2.01	97.94
10	0.19	1.34	99.28
11	0.05	0.39	99.67
12	0.03	0.21	99.88
13	0.01	0.09	99.97
14	0.00	0.03	100.00

538

539 **Table 4.** The loading factors of the indicators associated with each principal component.

540

Indicators	PC1	PC2	PC3	PC4	PC5
GR ($X_{1,\ norm}$)	−0.1974	0.1626	−0.3749	0.1147	0.0017
DT ($X_{2,\ norm}$)	−0.3106	−0.3036	0.2988	−0.2274	0.0252
DEN ($X_{3,\ norm}$)	−0.1240	0.1862	−0.4289	0.0915	−0.0251
Vp ($X_{4,\ norm}$)	0.4742	0.1086	0.2118	0.0630	−0.0833
V_s ($X_{5,\ norm}$)	0.4226	0.2656	−0.1703	0.2359	−0.0001
V_p/V_s ($X_{6,\ norm}$)	0.5210	0.0291	0.1389	0.1321	0.0251
RT ($X_{7,\ norm}$)	−0.1677	0.2760	−0.4075	0.1175	−0.0469
GR_slope ($X_{8,\ norm}$)	−0.1080	−0.0259	0.1570	0.4090	0.5451
DT_slope ($X_{9,\ norm}$)	0.2016	−0.3665	−0.3183	−0.1926	0.2956
DEN_slope ($X_{10,\ norm}$)	−0.1358	0.0842	0.1574	0.3917	0.5301
V_p_slope ($X_{11,\ norm}$)	−0.0776	0.3820	0.0964	−0.3432	0.3063
V_s_slope ($X_{12,\ norm}$)	−0.1673	0.4370	0.3240	0.0225	−0.2097
V_p/V_s_slope ($X_{13,\ norm}$)	−0.0012	0.4513	0.1578	−0.3270	0.1269
RT_slope ($X_{14,\ norm}$)	−0.2035	−0.0690	0.1924	0.5029	−0.4117

541

Leveraging the component transformation matrix (Table 4), we construct linear equations for the five principal components through multivariate regression (Eqs. (4)–(8)). The eigenvalues' variance contributions are then assigned as weighting coefficients to derive a composite scoring function (Eq. (9)). Cross-plot analysis between comprehensive scores and methane carbon isotope gradients across depth intervals demonstrates a robust parametric correlation (R^2 = 0.7803) (Fig. 10). Notably, when the comprehensive score exceeds a threshold of 2, the methane carbon isotope gradient increases sharply, suggesting a significant enhancement in sealing capacity. This relationship confirms that conventional well-log attributes and their derivative slope parameters can be quantitatively integrated via PCA into a reliable proxy for methane carbon isotope gradients, thereby enabling predictive assessment of sealing capacity in hydrate-bearing formations.

$$F_1 = -0.1974X_{1,\mathrm{norm}} - 0.3106X_{2,\mathrm{norm}} - 0.1240X_{3,\mathrm{norm}} + \mathrm{L} - 0.2035X_{14,\mathrm{norm}} \quad (4)$$

$$F_2 = 0.1626X_{1,\mathrm{norm}} - 0.3036X_{2,\mathrm{norm}} + 0.1862X_{3,\mathrm{norm}} + \mathrm{L} - 0.0690X_{14,\mathrm{norm}} \quad (5)$$

$$F_3 = -0.3749X_{1,\mathrm{norm}} + 0.2988X_{2,\mathrm{norm}} - 0.4289X_{3,\mathrm{norm}} + \mathrm{L} + 0.1924X_{14,\mathrm{norm}} \quad (6)$$

$$F_4 = 0.1147X_{1,\mathrm{norm}} - 0.2274X_{2,\mathrm{norm}} + 0.0915X_{3,\mathrm{norm}} + \mathrm{L} + 0.5029X_{14,\mathrm{norm}} \quad (7)$$

$$F_5 = 0.0017X_{1,\mathrm{norm}} + 0.0252X_{2,\mathrm{norm}} - 0.0251X_{3,\mathrm{norm}} + \mathrm{L} - 0.4117X_{14,\mathrm{norm}} \quad (8)$$

$$F_C = 0.2217F_1 + 0.2164F_2 + 0.1845F_3 + 0.1657F_4 + 0.0519F_5 \quad (9)$$

where F_1–F_5: scores of the first to fifth principal components (PC1–PC5), respectively; F_C: composite score (weighted sum of PC scores). $X_{1,\mathrm{norm}}$–$X_{14,\mathrm{norm}}$

represent the min–max normalized values of GR, DT, DEN, V_p, V_s, V_p/V_s ratio, RT, and their respective slope parameters (GR_slope, DT_slope, DEN_slope, V_p_slope, V_s_slope, V_p/V_s_slope, RT_slope).

Fig. 10. Crossplot of the comprehensive score obtained from PCA and the methane carbon isotope gradient.

To further explore the relationship between changes in methane carbon isotope gradients and formation sealing, we compiled methane carbon isotope gradients and corresponding gas saturation data from multiple wells in the study area. The results demonstrate a clear positive correlation, in which intervals with higher $\delta^{13}C_1$ gradients consistently correspond to increased gas saturations (Fig. 11). Notably, when the gradient reaches approximately 0.5‰/m, the gas saturation exceeds 50%, marking a critical inflection point in reservoir performance. This threshold therefore provides a practical diagnostic criterion for distinguishing intervals with effective sealing capacity. Furthermore, the observed consistency between isotopic gradients and gas saturation strongly supports the theoretical link between vertical isotopic enrichment and the suppression of upward gas leakage. Importantly, because $\delta^{13}C_1$ gradients can be predicted indirectly through diagnostic well-log responses and integrated PCA models, this approach offers a novel means of forecasting sealing capacity in unconsolidated, hydrate-bearing sediments where direct core measurements are often unavailable.

584

585 **Fig. 11.** Crossplot of methane carbon isotope gradient at the top of the gas layer and its
586 gas saturation.

587

588 *5.3. Natural gas accumulation mechanisms and modeling*

589 Mounting evidence identifies marine gas hydrates as a critical climate feedback
590 element sensitive to global warming (Kvenvolden, 1993; Maslin et al., 2010). These
591 metastable deposits exhibit high susceptibility to temperature-pressure perturbations,
592 with potential methane release posing dual threats of accelerated climate forcing and
593 geohazards to offshore operations (Majorowicz et al., 2014; Hassanpouryouzband et al.,
594 2020). Conversely, hydrate formation can enhance sealing capacity, promoting the
595 accumulation of underlying hydrocarbon accumulations. Our study focuses on the
596 Ledong Formation within a deepwater gas hydrate stability zone (Fig. 12(a)).
597 Thermogenic gas migration displays an NE-to-SW vector, with northwestern sectors
598 exhibiting higher thermogenic fractions (55%–73%) (Fig. 7), indicating preferential
599 migration pathways along structural trends.

600

601 **Fig. 12.** Methane distribution and main migration directions of thermogenic gas in the
602 study area **(a)** (revised from Ruppel and Kessler, 2017). Conceptual model of gas
603 accumulation through unconsolidated Quaternary hydrate-bearing sediments, and
604 modeled variations in the capillary-dependent methane carbon isotope (solid blue line)

and methane carbon isotope gradient (dashed green line) below the seafloor **(b)**. Fig. 12(b) is a further explanation of the position of the dotted blue box in Fig. 12(a).

The effective migration system is the key factor controlling large-scale gas accumulation in the Lingshui 36-1 submarine fan, given that the underlying source rocks have not reached the threshold for significant hydrocarbon generation and that the field is located ~35 km laterally and ~4 km vertically away from the gas kitchen of the Yacheng Formation. Since the Neogene, sufficient sediment supply in the western QDNB led to continuous progradation of the shelf break, southward migration of axial canyon systems, and repeated erosion–fill processes of turbidity currents. The subsequent canyon-fill complexes and overspill deposits connected laterally and vertically, forming a relay-like “bowl-shaped” transfer station for gas migration. This transfer station initially accumulated thermogenic gas but was later tilted northwestward due to differential subsidence, creating a “northwest low–southeast high” geometry that favored gas leakage toward the Lingshui 36-1 fan. Consequently, mature thermogenic gas generated in the Yacheng Formation migrated laterally through the canyon-related stacked sand bodies into the Ledong submarine fan (Fig. 13). In addition, local gas chimneys, fractures, and faults in the Lingnan low-uplift area provided vertical pathways for shallow microbial gas to charge the ultra-shallow Ledong fan (Xu et al., 2025). Within the fan, early-stage lower sand bodies were dissected and partially breached, enabling upward redistribution of gas. The overlying mud-rich channels

626 further promoted the development of a NE–SW-trending structural ridge at the fan top,
627 along which gas migrated from the middle- to low-position sand bodies toward the ridge
628 culminations (Fig. 13). Lateral juxtaposition between the Ledong and Yinggehai fans
629 provided favorable migration conditions in the central and eastern fan blocks, whereas
630 migration into the western block was relatively restricted. This is supported by methane
631 isotopic values: gases from the western high-position wells (W1, W7) show lighter
632 isotopic values (–66.7‰ to –55.7‰), indicating a dominant microbial origin, while
633 gases from the central and eastern high-position wells (W3, W6) exhibit heavier $\delta^{13}C_1$
634 values (–47.9‰ to –43.8‰), reflecting a mixed microbial–thermogenic signature. These
635 results confirm that mature thermogenic gas migrated from the central canyon system
636 into the eastern and central fan blocks, consistent with the structural and sedimentary
637 migration pathways delineated from seismic and stratigraphic interpretations.
638
639 **Fig. 13.** The top structural map of the Ledong Formation in the study area and the
640 distribution of submarine fans of the Yinggehai Formation and Ledong Formation
641 nearby.
642
643 The methane recycling theory has been proposed to explain the coexistence of
644 enriched hydrate accumulations within the BGHSZ and underlying free gas (You et al.,
645 2019). During sediment burial, hydrates traversing the BGHSZ dissociate into free gas
646 and water (Fig. 12(b)). When gas volumes exceed capillary displacement thresholds, a

portion of free gas migrates upward, recycling into the BGHSZ to form secondary hydrate accumulations—particularly when supplemented by thermogenic gas fluxes. Early models assumed that free gas released by hydrate decomposition would reform hydrates in the BGHSZ (Xu and Ruppel, 1999). Consequently, pore-occluding hydrate layers develop, inhibiting vertical gas migration and promoting further hydrate growth above the BGHSZ. This self-sealing mechanism persists until seal breaching reinitiates free gas flow. Critically, the seal capacity of the caprock is governed by hydrate morphology and saturation, with cementing habits imposing greater flow barriers than pore-filling types.

This study incorporates the mechanism of buoyancy-driven vertical migration of free gas through hydrate-bearing caprocks by analyzing methane carbon isotope (δ^{13}C-CH_4) signatures and their gradient variations. Vertically, the process can be delineated into four distinct stages (Fig. 12(b)): (1) Stage 1: Pore gas is dominated by microbial methane. Influenced by diffusive fractionation, δ^{13}C-CH_4 becomes progressively depleted (lighter) upwards, yielding a small positive δ^{13}C-CH_4 gradient. (2) Stage 2: At the sediment-hydrate interface, extensive hydrate formation within pores creates an effective seal. Beneath this barrier, the influx of thermogenic gas causes δ^{13}C-CH_4 to increase sharply (become heavier) with depth, producing a pronounced maximum in the δ^{13}C-CH_4 gradient. (3) Stage 3: Pore gas is primarily thermogenic gas. δ^{13}C-CH_4 stabilizes near its maximum value, resulting in a near-zero gradient. (4) Stage 4: Mixing occurs between deeper thermogenic gas (migrating under gravity) and

shallower diffusing microbial gas. This leads to δ^{13}C-CH_4 depletion (lighter values) with increasing depth, characterized by a small negative δ^{13}C-CH_4 gradient. The thickness of this effective sealing barrier ranges from <1 m to tens of meters, contingent upon pore-size distribution and the content of pore water and methane within the sediment. However, rigorous validation of this proposed mechanism requires detailed field observations and/or laboratory experiments focused on the nature and dynamics of the effective barrier.

In the absence of thermogenic gas input, methane carbon isotope (δ^{13}C-CH_4) values are consistently less than −55.0‰ throughout the profile. Influenced by diffusive fractionation, δ^{13}C-CH_4 becomes progressively depleted (lighter) upwards with decreasing burial depth. In contrast, the influx of thermogenic gas, facilitated by free gas migration, elevates hydrate saturation, leading to an increase in the thickness of the hydrate-enriched layer. The formation of this hydrate-enriched zone establishes a stable capillary barrier, promoting the accumulation of an interconnected underlying gas column (Fig. 12(b)). Within the effective seal interval defined by this barrier, δ^{13}C-CH_4 values increase sharply with increasing depth, concomitant with a pronounced maximum in the methane carbon isotope gradient. This isotopic signature reveals disconnected pores and throats within the sealing interval. Notably, not all hydrate-bearing intervals function as effective seals; the effective capillary barrier constitutes only a portion of the hydrate zone. Furthermore, the methane carbon isotope profile indicates that thermogenic gas migration occurs predominantly via lateral

pathways.

5.4. Implications for the sealing capacity of unconsolidated hydrate-bearing sediments

Gas hydrate dissociation represents a quantifiable climate risk due to its potential to release vast amounts of methane, a greenhouse gas with 28–34 times the warming potential of CO_2 over a 100-year timescale. Laboratory and numerical studies have shown that each unit volume of hydrate can generate ~164.6 volumes of methane gas and 0.87 volumes of water under standard conditions, producing rapid pore-pressure buildup and slope destabilization (Nixon and Grozic, 2007). Climate model simulations indicate that seafloor warming of only 2–4 ℃ could dissociate the entire upper-slope hydrate inventory off the Chilean margin within the next century, potentially releasing several gigatonnes of carbon and triggering slope failure (Alessandrini et al., 2019; Ruffine et al., 2023). Likewise, Arctic permafrost hydrates are highly sensitive to minor warming, with numerical modeling suggesting a lag of merely 20–30 years between the onset of warming and measurable methane release (O'Connor et al., 2010; Thatcher et al., 2013). Although microbial oxidation within sediments and the water column acts as a partial barrier to atmospheric transfer, catastrophic dissociation events such as the Storegga Slide demonstrate that abrupt methane injection into the atmosphere can occur when slope failures bypass these natural filters (Bugge et al., 1988; Maslin et al., 2010). Current estimates suggest that hydrate-related methane emissions may range from 0.1–1 Gt C during localized slope failures to several tens of gigatonnes of carbon under regional-scale destabilization, magnitudes sufficient to act as a positive feedback to

global warming (Ruppel and Kessler, 2017; Ruffine et al., 2023). Consequently, robust characterization of effective seals and their spatiotemporal sealing capacity is paramount for both hazard mitigation and sustainable resource development. Critically, targeted extraction from well-sealed intervals offers a dual benefit: converting geohazard-prone greenhouse gases into cleaner-burning energy resources while maintaining reservoir stability through controlled depressurization.

Our integrated geochemical and petrophysical analysis reveals that the sealing capacity of hydrate-bearing strata is dynamically recorded in gas composition profiles and methane carbon isotope gradients. Specifically: (1) Thermogenic influx elevates hydrate saturation, promoting capillary barrier formation and underlying gas column accumulation. (2) Sharp positive isotopic gradients (e.g., >0.5‰/m) at sediment-hydrate interfaces correlate with effective seals, reflecting arrested vertical migration and isotopic disequilibrium (Figs. 6 and 11). (3) Peak methane carbon isotope gradients (e.g., ~1866 m in well W4) denote zones of maximal pore-throat disconnection, while negative gradients below barriers indicate deeper thermogenic-microbial gas mixing (Fig. 9). These isotopic fractionation patterns provide a direct proxy for seal capacity, with gradient magnitudes scaling with gas saturation. Future studies should integrate core, well log, and seismic attributes to systematically predict spatial heterogeneities in sealing capacity across basin scales. This approach will optimize the identification of high-integrity seals for safer gas extraction and improved assessment of hydrate-associated carbon storage stability.

Although the coupled migration–trapping–remobilization model is established based on data from the Qiongdongnan Basin, its applicability extends beyond the study area. The framework captures fundamental controls—gas charging, isotopic fractionation, and sealing—that are common to hydrate systems worldwide (Milkov, 2005; Collett et al., 2009). Nevertheless, hydrate layers in other regions may originate from different mixtures of microbial and thermogenic gases, and the magnitude of isotopic oscillations depends strongly on local source input and seal integrity. Previous studies in the South China Sea have demonstrated that hydrates are dominantly sourced from microbial methane, with significant thermogenic contributions in fault-controlled or channelized reservoirs (Wu et al., 2011; Zhu et al., 2013; Lai et al., 2021). Therefore, direct application of the model to other basins requires site-specific calibration of gas sources, isotopic baselines, and seal capacity. With such adjustments, the model provides a robust and transferable framework for predicting and evaluating hydrate accumulations in diverse geological settings.

6. Conclusions

This study establishes methane carbon isotope gradients as a robust proxy for evaluating dynamic seal capacity in unconsolidated Quaternary hydrate-bearing sediments of the Qiongdongnan Basin. Key findings reveal:

(1) Vertical methane carbon isotope gradient (>0.5‰/m) quantitatively diagnoses effective capillary barriers within hydrate-bearing strata, with peak gradients correlating to zones of maximal pore-throat disconnection (e.g., 1866 m in well W4).

752 (2) A quantitative evaluation model for mixed gas sources is established, in which
753 the contribution of thermogenic gas in wells W6 and W8 is 55%–73%, while that in
754 well W1 is 28%–32%. Thermogenic gas influx elevates hydrate saturation, promoting
755 self-sealing through hydrate morphology transitions, which in turn trap underlying
756 mixed gas and form stacked accumulations.

757 (3) The novel PCA-integrated logging model (cumulative variance: 84.02%, R^2 =
758 0.78) bridges geochemical signatures with petrophysical properties, enabling prediction
759 of seal capacity where direct measurements are unfeasible.

760 These mechanisms underpin a "charge-dynamic barrier-mixing" model in which
761 the influx of these thermogenic gases that migrate buoyantly, forms dynamic capillary
762 barriers within the hydrate stability zone, trapping underlying microbial gases through
763 buoyancy-driven migration and mixing. This process is documented in diagnostic
764 methane carbon isotope and its gradient profiles, highlighting the dual role of
765 hydrate-bearing sediments as carbon sinks and geohazard sources. Future work should
766 integrate seismic attributes to scale the proxy for basin-wide seal integrity mapping,
767 optimizing both gas hydrate exploitation and climate-risk mitigation in rapidly
768 deposited marginal basins.

769 **Acknowledgments**

770 The authors sincerely thank the Hainan Branch of CNOOC (China) Limited for
771 providing data collection services. This work was financially supported by the
772 Postdoctoral Fellowship Program of CPSF (Grant No. GZC20242002), China, the

Science Foundation of China University of Petroleum, Beijing (Grant No. 2462024XKBH005), China, the National Science and Technology Major Project of the Ministry of Science and Technology of China (2025ZD1402707), and the 2021 AAPG Foundation Grants-in-Aid Program (Roger W. Stoneburner Memorial Grant), United States. We thank Editor Min Li and the other two anonymous reviewers for their detailed comments, which significantly improved the manuscript.

References

Abdi, H., Williams, L.J., 2010. Principal component analysis. Wiley interdisciplinary reviews: computational statistics 2(4), 433-459. https://doi.org/10.1002/wics.101.

Alessandrini, G., Tinivella, U., Giustiniani, M., et al., 2019. Potential instability of gas hydrates along the Chilean margin due to ocean warming. Geosciences 9(5), 234. https://doi.org/10.3390/geosciences9050234.

Archer, D., 2007. Methane hydrate stability and anthropogenic climate change. Biogeosciences 4(4), 521-544. https://doi.org/10.5194/bg-4-521-2007.

Barker, J.F., Fritz, P., 1981. Carbon isotope fractionation during microbial methane oxidation. Nature 293(5830), 289-291. https://doi.org/10.1038/293289a0.

Berner, U., Faber, E., 1988. Maturity related mixing model for methane, ethane and propane, based on carbon isotopes. Organic Geochemistry 13(1-3), 67-72. https://doi.org/10.1016/0146-6380(88)90026-5.

Boswell, R., Collett, T.S., 2011. Current perspectives on gas hydrate resources. Energy & environmental science 4(4), 1206-1215. https://doi.org/10.1039/C0EE00203H.

794 Bourg, I.C., Ajo-Franklin, J.B., 2017. Clay, water, and salt: controls on the permeability
795 of fine-grained sedimentary rocks. Accounts of chemical research 50(9),
796 2067-2074. https://doi.org/10.1021/acs.accounts.7b00261.
797 Bray, J.D., Macedo, J., 2023. Performance-based seismic assessment of slope systems.
798 Soil Dynamics and Earthquake Engineering 168, 107835.
799 https://doi.org/10.1016/j.soildyn.2023.107835.
800 Brook, E., Archer, D., Frolking, S., et al., Potential for abrupt changes in atmospheric
801 methane, pp. 163-201 in U.S. Climate Change Science Program Synthesis and
802 Assessment Product 3.4: Abrupt Climate Change. A report by the U.S. Climate
803 Change Science Program and the Subcommittee on Global Change Research, U.S.
804 Geological Survey, Reston VA.
805 Bugge, T., Belderson, R.H., Kenyon, N.H., 1988. The storegga slide. Philosophical
806 Transactions of the Royal Society of London. Series A, Mathematical and Physical
807 Sciences 325(1586), 357-388.
808 https://ui.adsabs.harvard.edu/link_gateway/1988RSPTA.325..357B/doi:10.1098/rst
809 a.1988.0055.
810 Cao, H., Jin, S., Hou, M., et al., 2022. Astronomical cycles calibrated the sea-level
811 sequence durations of Late Miocene to Pliocene in Qiongdongnan Basin, south
812 China sea. Marine and Petroleum Geology 143, 105813.
813 https://doi.org/10.1016/j.marpetgeo.2022.105813.
814 Chen, Y., Jiao, Y., Chen, X., et al., 2025. Quantitative assessment of natural gas

geochemical characteristics and mixed source contributions in the Qixia Formation, central Sichuan Basin. Natural Gas Geoscience 36(4), 677-688. https://doi.org/10.11764/j.issn.1672-1926.2024.09.004 (in chinese).

Chung, H.M., Sackett, W.M., 1979. Use of stable carbon isotope compositions of pyrolytically derived methane as maturity indices for carbonaceous materials. Geochimica et Cosmochimica Acta, 43(12). https://doi.org/10.1016/0016-7037(79)90010-3.

Collett, T.S., Johnson, A.H., Knapp, C.C., et al., 2009. Natural gas hydrates: A review. AAPG Bulletin 93(6), 809–840. https://doi.org/10.1306/13201142M891602.

Collett, T.S., Lee, M.W., 2012. Well log characterization of natural gas-hydrates. Petrophysics 53(05): 348-367.

Dai, J., Li, J., Luo, X., et al., 2005. Stable carbon isotope compositions and source rock geochemistry of the giant gas accumulations in the Ordos Basin, China. Organic Geochemistry 36(12), 1617-1635. https://doi.org/10.1016/j.orggeochem.2005.08.017.

Dean, J.F., Middelburg, J.J., Röckmann, T., et al., 2018. Methane feedbacks to the global climate system in a warmer world. Reviews of Geophysics 56(1), 207-250. https://doi.org/10.1002/2017RG000559.

Feng, Y., Qu, A., Han, Y., et al., 2023. Effect of gas hydrate formation and dissociation on porous media structure with clay particles. Applied Energy 349, 121694. https://doi.org/10.1016/j.apenergy.2023.121694.

836 Fisher, A.T., 2005. Marine hydrogeology: recent accomplishments and future
837 opportunities. Hydrogeology Journal 13, 69-97.
838 https://doi.org/10.1007/s10040-004-0400-y.
839 Hassanpouryouzband, A., Joonaki, E., Farahani, M.V., et al., 2020. Gas hydrates in
840 sustainable chemistry. Chemical society reviews 49(15), 5225-5309.
841 https://doi.org/10.1039/C8CS00989A.
842 Hu, G., Zhang, Z., Zhao, Y., et al., 2024. Formation mechanism and geophysical
843 properties of fracture-filling gas hydrate in the host sediments: A comprehensive
844 review. Earth-Science Reviews, 104917.
845 https://doi.org/10.1016/j.earscirev.2024.104917.
846 Huang, B., Tian, H., Li, X., et al., 2016. Geochemistry, origin and accumulation of
847 natural gases in the deepwater area of the Qiongdongnan Basin, South China Sea.
848 Marine and Petroleum Geology 72, 254-267.
849 https://doi.org/10.1016/j.marpetgeo.2016.02.007.
850 IEA., 2024. World Energy Outlook 2024.
851 https://www.iea.org/reports/world-energy-outlook-2024.
852 Jolliffe, I.T., Cadima, J., 2016. Principal component analysis: a review and recent
853 developments. Philosophical transactions of the royal society A: Mathematical,
854 Physical and Engineering Sciences 374(2065), 20150202.
855 https://doi.org/10.1098/rsta.2015.0202.
856 Joye, S.B., MacDonald, I.R., Montoya, J.P., et al., 2005. Geophysical and geochemical

857 signatures of Gulf of Mexico seafloor brines. Biogeosciences 2(3), 295-309.
858 https://doi.org/10.5194/bg-2-295-2005.
859 Kasala, E.E., Wang, J., Mkono, C.N., et al., 2024. Systematic Review and Perspectives
860 of Methane (CH4) Classifications and Production Methods from CH4 Hydrate
861 Reservoirs. Energy & Fuels 38(20), 19293-19335.
862 https://doi.org/10.1021/acs.energyfuels.4c03427.
863 Klauda, J.B., Sandler, S.I., 2005. Global distribution of methane hydrate in ocean
864 sediment. Energy & Fuels 19(2), 459-470. https://doi.org/10.1021/ef049798o.
865 Kong, W., Wu, C., Zhang, Y., et al., 2025. Fault-driven stress field variations as
866 predictors of bedrock landslide distribution patterns. Landslides, 1-20.
867 https://doi.org/10.1007/s10346-025-02475-1.
868 Kvenvolden, K.A., 1993. Gas hydrates—geological perspective and global change.
869 Reviews of geophysics 31(2), 173-187. https://doi.org/10.1029/93RG00268.
870 Lai, H., Fang, Y., Kuang, Z., et al., 2021. Geochemistry, origin and accumulation of
871 natural gas hydrates in the Qiongdongnan Basin, South China Sea: Implications
872 from site GMGS5-W08. Marine and Petroleum Geology 123, 104774.
873 https://doi.org/10.1016/j.marpetgeo.2020.104774.
874 Lai, H., Lu, Q., Yang, Z., et al., 2024. Origin and microbial degradation of thermogenic
875 hydrocarbons within the sandy gas hydrate reservoirs in the Qiongdongnan Basin,
876 northern South China Sea. Marine and Petroleum Geology 165, 106871.
877 https://doi.org/10.1016/j.marpetgeo.2024.106871.

878 Lai, H., Qiu, H., Kuang, Z., et al., 2022. Integrated signatures of secondary microbial
879 gas within gas hydrate reservoirs: A case study in the Shenhu area, northern South
880 China Sea. Marine and Petroleum Geology 136, 105486.
881 https://doi.org/10.1016/j.marpetgeo.2021.105486.
882 Liu, K., Cheng, P., Tian, H., et al., 2023. Development model of shallow lithologic traps
883 and natural gas accumulation mechanisms in marine deep-water areas: A case
884 study in the Qiongdongnan basin, south China sea. Marine and Petroleum Geology
885 151, 106211. https://doi.org/10.1016/j.marpetgeo.2023.106211.
886 Liu, Q., Wu, X., Wang, X., et al., 2019. Carbon and hydrogen isotopes of methane,
887 ethane, and propane: A review of genetic identification of natural gas.
888 Earth-Science Reviews 190, 247-272.
889 https://doi.org/10.1016/j.earscirev.2018.11.017.
890 Lüdmann, T., Wong, H.K., Wang, P., 2001. Plio–Quaternary sedimentation processes
891 and neotectonics of the northern continental margin of the South China Sea.
892 Marine Geology 172(3-4), 331-358.
893 https://doi.org/10.1016/S0025-3227(00)00129-8.
894 Mahabadi, N., Dai, S., Seol, Y., et al., 2019. Impact of hydrate saturation on water
895 permeability in hydrate-bearing sediments. Journal of petroleum science and
896 engineering 174, 696-703. https://doi.org/10.1016/j.petrol.2018.11.084.
897 Majorowicz, J., Grasby, S.E., Safanda, J., et al., 2014. Gas hydrate contribution to Late
898 Permian global warming. Earth and Planetary Science Letters 393, 243-253.

https://doi.org/10.1016/j.epsl.2014.03.003.

Marín‐Moreno, H., Minshull, T.A., Westbrook, G.K., et al., 2015. Estimates of future warming‐induced methane emissions from hydrate offshore west S valbard for a range of climate models. Geochemistry, Geophysics, Geosystems 16(5), 1307-1323. https://doi.org/10.1002/2015GC005737.

Marín‐Moreno, H., Minshull, T.A., Westbrook, G.K., et al., 2013. The response of methane hydrate beneath the seabed offshore Svalbard to ocean warming during the next three centuries. Geophysical Research Letters 40(19), 5159-5163. https://doi.org/10.1002/grl.50985.

Maslin, M., Owen, M., Betts, R., et al., 2010. Gas hydrates: past and future geohazard?. Philosophical Transactions of the Royal Society A: Mathematical, Physical and Engineering Sciences 368(1919), 2369-2393. https://doi.org/10.1098/rsta.2010.0065.

Maslin, M., Owen, M., Day, S., et al., 2004. Linking continental-slope failures and climate change: Testing the clathrate gun hypothesis. Geology 32(1), 53-56. https://doi.org/10.1130/G20114.1.

McConnell, D.R., Zhang, Z., Boswell, R., 2012. Review of progress in evaluating gas hydrate drilling hazards. Marine and Petroleum Geology 34(1), 209-223. https://doi.org/10.1016/j.marpetgeo.2012.02.010.

Milkov, A.V., 2005. Molecular and stable isotope compositions of natural gas hydrates: A revised global dataset and basic interpretations in the context of geological

settings. Organic geochemistry 36(5), 681-702. https://doi.org/10.1016/j.orggeochem.2005.01.010.

Milkov, A.V., Etiope, G., 2018. Revised genetic diagrams for natural gases based on a global dataset of > 20,000 samples. Organic geochemistry 125, 109-120. https://doi.org/10.1016/j.orggeochem.2018.09.002.

Moridis, G.J.J., Collett, T.S.S., Pooladi-Darvish, M., et al., 2011. Challenges, uncertainties, and issues facing gas production from gas-hydrate deposits. SPE reservoir evaluation & engineering 14(01), 76-112. https://doi.org/10.2118/131792-PA.

Neuzil, C.E., 2019. Permeability of clays and shales. Annual Review of Earth and Planetary Sciences 47(1), 247-273. https://doi.org/10.1146/annurev-earth-053018-060437.

Nixon, M.F., Grozic, J.L.H., 2007. Submarine slope failure due to gas hydrate dissociation: a preliminary quantification. Canadian Geotechnical Journal 44(3), 314-325. https://doi.org/10.1139/t06-121.

O'Connor, F.M., Boucher, O., Gedney, N., et al., 2010. Possible role of wetlands, permafrost, and methane hydrates in the methane cycle under future climate change: A review. Reviews of Geophysics 48(4). https://doi.org/10.1029/2010RG000326.

Passchier, S., 2000. Soft-sediment deformation features in core from CRP-2/2A, Victoria Land Basin, Antarctica. Terra Antartica 7(3), 401-412.

941 http://hdl.handle.net/10013/epic.28263.d001.

942 Pei, J., Liu, E., Song, P., et al., 2024. Influencing Factors and Model of Shallow Gas
943 Enrichment in the Quaternary Sediments of the Qiongdongnan Basin, South China
944 Sea. Journal of Marine Science and Engineering 12(11), 1928.
945 https://doi.org/10.3390/jmse12111928.

946 Ren, J., Cheng, C., Xiong, P., et al., 2022. Sand-rich gas hydrate and shallow gas
947 systems in the Qiongdongnan Basin, northern South China Sea. Journal of
948 Petroleum Science and Engineering 215, 110630.
949 https://doi.org/10.1016/j.petrol.2022.110630.

950 Rice, D.D., Claypool, G.E., 1981. Generation, accumulation, and resource potential of
951 biogenic gas. AAPG bulletin 65(1), 5-25.
952 https://doi.org/10.1306/2F919765-16CE-11D7-8645000102C1865D.

953 Riedel, M., Freudenthal, T., Bialas, J., et al., 2021. In-situ borehole temperature
954 measurements confirm dynamics of the gas hydrate stability zone at the upper
955 Danube deep sea fan, Black Sea. Earth and Planetary Science Letters 563: 116869.
956 https://doi.org/10.1016/j.epsl.2021.116869.

957 Ruffine, L., Tang, A.M., O'neill, N., et al., 2023. Environmental challenges related to
958 methane hydrate decomposition from climate change scenario and anthropic
959 activities: State of the art, potential consequences and monitoring solutions.
960 Earth-Science Reviews 246, 104578.
961 https://doi.org/10.1016/j.earscirev.2023.104578.

962 Ruppel, C.D., Kessler, J.D., 2017. The interaction of climate change and methane
963 hydrates. Reviews of Geophysics 55(1), 126-168.
964 https://doi.org/10.1002/2016RG000534.
965 Ruppel, C.D., 2011. Methane hydrates and contemporary climate change. Nature
966 Eduction Knowledge 2(12), 12.
967 Schoell, M., 1983. Genetic characterization of natural gases. AAPG bulletin 67(12),
968 2225-2238. https://doi.org/10.1306/AD46094A-16F7-11D7-8645000102C1865D.
969 Scott, A.R., Kaiser, W.R., Ayers, Jr.W.B., 1994. Thermogenic and secondary biogenic
970 gases, San Juan Basin, Colorado and New Mexico—implications for coalbed gas
971 producibility. AAPG bulletin 78(8), 1186-1209.
972 https://doi.org/10.1306/A25FEAA9-171B-11D7-8645000102C1865D.
973 Sellm, M.S., Sloan, E.D., 1990. Hydrate dissociation in sediment. SPE Reservoir
974 Engineering 5(02), 245-251. https://doi.org/10.2118/16859-PA.
975 Shi, X., Jiang, H., Yang, J., et al., 2017. Models of the rapid post‐rift subsidence in the
976 eastern Qiongdongnan Basin, South China Sea: Implications for the development
977 of the deep thermal anomaly. Basin Research 29(3), 340-362.
978 https://doi.org/10.1111/bre.12179.
979 Snowdon, L.R., 2001. Natural gas composition in a geological environment and the
980 implications for the processes of generation and preservation. Organic
981 Geochemistry 32(7), 913-931. https://doi.org/10.1016/S0146-6380(01)00051-1.
982 Stolper, D.A., Lawson, M., Davis, C.L., et al., 2014. Formation temperatures of

983 thermogenic and biogenic methane. Science 344(6191), 1500-1503.
984 https://doi.org/10.1126/science.1254509.
985 Su, A., Chen, H., Feng, Y., et al., 2023. Distal accumulation of leaked gas from deep
986 overpressured zone: the case of the Yanan Sag, Qiongdongnan Basin, South China
987 Sea. Marine and Petroleum Geology 151, 106181.
988 https://doi.org/10.1016/j.marpetgeo.2023.106181.
989 Su, L., Zheng, J., Chen, G., et al., 2012. The upper limit of maturity of natural gas
990 generation and its implication for the Yacheng formation in the Qiongdongnan
991 Basin, China. Journal of Asian Earth Sciences 54, 203-213.
992 https://doi.org/10.1016/j.jseaes.2012.04.016.
993 Sun, H., Chen, B., Yang, Z., et al., 2022. Natural gas hydrate accumulation mechanisms
994 considering the multi-phase seepage and exploitation disturbance in porous media.
995 Fuel 330, 125687. https://doi.org/10.1016/j.fuel.2022.125687.
996 Thatcher, K.E., Westbrook, G.K., Sarkar, S., et al., 2013. Methane release from warming
997 - induced hydrate dissociation in the West Svalbard continental margin: Timing,
998 rates, and geological controls. Journal of Geophysical Research: Solid Earth 118(1),
999 22-38. https://doi.org/10.1029/2012JB009605.
1000 Tishchenko, P., Hensen, C., Wallmann, K., et al, 2005. Calculation of the stability and
1001 solubility of methane hydrate in seawater. Chemical geology 219(1-4), 37-52.
1002 https://doi.org/10.1016/j.chemgeo.2005.02.008.
1003 Waite, W.F., Santamarina, J.C., Cortes, D.D., et al., 2009. Physical properties of hydrate

- bearing sediments. Reviews of geophysics 47(4). https://doi.org/10.1029/2008RG000279.

Wei, J., Wu, T., Zhu, L., et al., 2021. Mixed gas sources induced co-existence of sI and sII gas hydrates in the Qiongdongnan Basin, South China Sea. Marine and Petroleum Geology 128, 105024. https://doi.org/10.1016/j.marpetgeo.2021.105024.

Wold, S., Esbensen, K., Geladi, P., 1987. Principal component analysis. Chemometrics and intelligent laboratory systems 2(1-3), 37-52. https://doi.org/10.1016/0169-7439(87)80084-9.

Wu, N., Zhang, H., Yang, S., et al., 2011. Gas hydrate system of Shenhu area, northern South China Sea: geochemical results. Journal of Geological Research 2011(1), 370298. https://doi.org/10.1155/2011/370298.

Xia, X., Tang, Y., 2012. Isotope fractionation of methane during natural gas flow with coupled diffusion and adsorption/desorption. Geochimica et Cosmochimica Acta 77, 489-503. https://doi.org/10.1016/j.gca.2011.10.014.

Xiao, X.M., Xiong, M., Tian, H., et al., 2006. Determination of the source area of the Ya13-1 gas pool in the Qiongdongnan Basin, South China Sea. Organic Geochemistry 37(9), 990-1002. https://doi.org/10.1016/j.orggeochem.2006.06.001.

Xu, C., Wu, K., Pei, J., et al., 2025. Enrichment mechanisms and accumulation model of ultra-deep water and ultra-shallow gas: A case study of Lingshui 36-1 gas field in Qiongdongnan Basin, South China Sea. Petroleum Exploration and Development

52(1), 50-63. https://doi.org/10.1016/S1876-3804(25)60004-8.

Xu, W., Ruppel, C., 1999. Predicting the occurrence, distribution, and evolution of methane gas hydrate in porous marine sediments. Journal of Geophysical Research: Solid Earth 104(B3), 5081-5095. https://doi.org/10.1029/1998JB900092.

Ye, J., Wei, J., Liang, J., et al., 2019. Complex gas hydrate system in a gas chimney, South China Sea. Marine and Petroleum Geology 104, 29-39. https://doi.org/10.1016/j.marpetgeo.2019.03.023.

Ye, Q., Mei, L., Shi, H., et al., 2018. The Late Cretaceous tectonic evolution of the South China Sea area: An overview, and new perspectives from 3D seismic reflection data. Earth-Science Reviews 187, 186-204. https://doi.org/10.1016/j.earscirev.2018.09.013.

Yoshimoto, N., Wu, Q., Fujita, K., et al., 2023. Hydrate dissociation and mechanical properties of hydrate-bearing sediments under local thermal stimulation conditions. Gas Science and Engineering 116, 205045. https://doi.org/10.1016/j.jgsce.2023.205045.

You, K., Flemings, P.B., Malinverno, A., et al., 2019. Mechanisms of methane hydrate formation in geological systems. Reviews of Geophysics 57(4), 1146-1196. https://doi.org/10.1029/2018RG000638.

Yuan, Y., Zhu, W., Mi, L., et al., 2009. “Uniform geothermal gradient” and heat flow in the Qiongdongnan and Pearl River Mouth Basins of the South China Sea. Marine and Petroleum Geology 26(7), 1152-1162.

https://doi.org/10.1016/j.marpetgeo.2008.08.008.

Zhang, G., Qu, H., Jia, Q., et al., 2021. Passive continental margin segmentation of the marginal seas and its effect on hydrocarbon accumulation: A case study of the northern continental margin in South China Sea. Marine and Petroleum Geology 123, 104741. https://doi.org/10.1016/j.marpetgeo.2020.104741.

Zhang, G., Zhang, Y., Shen, H., et al., 2014. An analysis of natural gas exploration potential in the Qiongdongnan Basin by use of the theory of "joint control of source rocks and geothermal heat". Natural Gas Industry B 1(1), 41-50. https://doi.org/10.1016/j.ngib.2014.10.005.

Zhang, J., Yan, D., Pei, J., et al., 2025. Shallow gas accumulation mechanism in the Qiongdongnan Basin, South China Sea. Marine and Petroleum Geology, 107389. https://doi.org/10.1016/j.marpetgeo.2025.107389.

Zhang, T., Krooss, B.M., 2001. Experimental investigation on the carbon isotope fractionation of methane during gas migration by diffusion through sedimentary rocks at elevated temperature and pressure. Geochimica et Cosmochimica Acta 65(16), 2723-2742. https://doi.org/10.1016/S0016-7037(01)00601-9.

Zhao, G., Zheng, J., Gong, G., et al., 2023. Formation characteristics and leakage termination effects of CO2 hydrate cap in case of geological sequestration leakage. Applied Energy 351, 121896. https://doi.org/10.1016/j.apenergy.2023.121896.

Zhu, H.Y., Dang, Y.K., Wang, G.R., et al., 2021. Near-wellbore fracture initiation and propagation induced by drilling fluid invasion during solid fluidization mining of

1067 submarine nature gas hydrate sediments. Petroleum Science 18(6), 1739-1752.
1068 https://doi.org/10.1016/j.petsci.2021.09.026.
1069 Zhu, W., Shi, H., Huang, B., et al., 2021. Geology and geochemistry of large gas fields
1070 in the deepwater areas, continental margin basins of northern South China Sea.
1071 Marine and Petroleum Geology 126, 104901.
1072 https://doi.org/10.1016/j.marpetgeo.2021.104901.
1073 Zhu, Y.H., Xia, H., Fu, S.Y., et al., 2013. Gas sources of natural gas hydrates in the
1074 Shenhu Drilling Area, South China Sea: geochemical evidence and geological
1075 analysis. Acta Geologica Sinica - English Edition 87(3), 767-776.
1076 https://doi.org/10.1111/1755-6724.12088.
1077

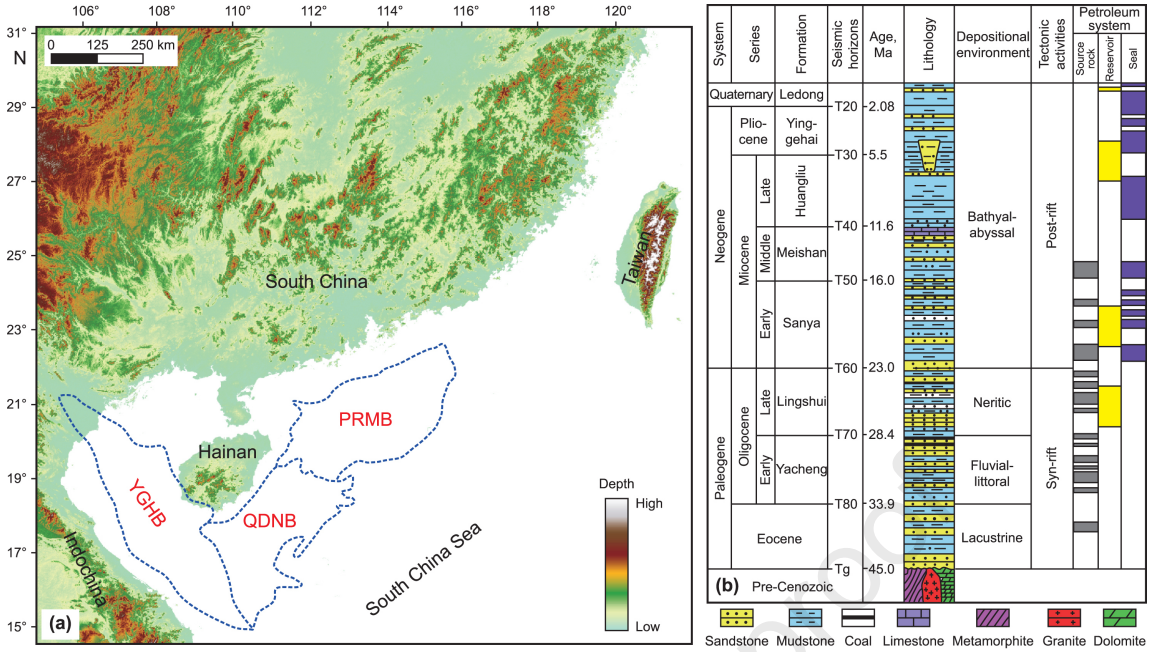
106°
108°
110°
112°
114°
116°
118°
120°
31°
29°
27°
25°
23°
21°
19°
17°
15°
N
0 125 250 km
South China
Taiwan
PRMB
Hainan
YGHB
QDNB
Indochina
South China Sea
Depth
High
Low
(a)
System
Series
Formation
Seismic horizons
Age, Ma
Lithology
Depositional environment
Tectonic activities
Petroleum system
Source rock
Reservoir
Seal
Quaternary
Ledong
Neogene
Plio-cene
Ying-gehai
Miocene
Late
Huangliu
Middle
Meishan
Early
Sanya
Paleogene
Oligocene
Late
Lingshui
Early
Yacheng
Eocene
Pre-Cenozoic
T20
T30
T40
T50
T60
T70
T80
Tg
2.08
5.5
11.6
16.0
23.0
28.4
33.9
45.0
Bathyal-abyssal
Neritic
Fluvial-littoral
Lacustrine
Post-rift
Syn-rift
(b)
Sandstone
Mudstone
Coal
Limestone
Metamorphite
Granite
Dolomite

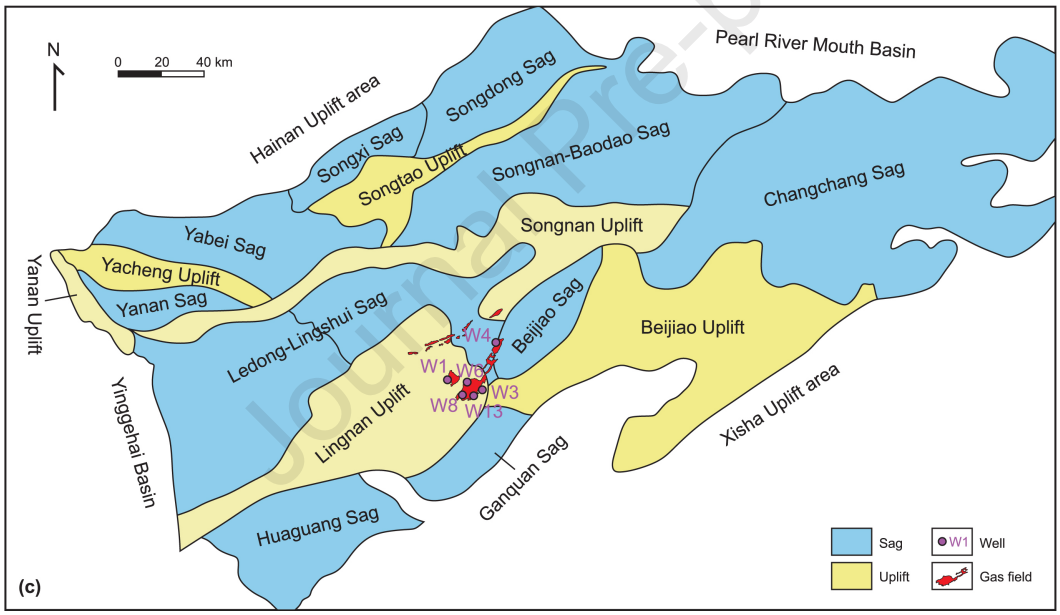
N
0 20 40 km
Pearl River Mouth Basin
Hainan Uplift area
Songdong Sag
Songxi Sag
Songtao Uplift
Songnan-Baodao Sag
Changchang Sag
Songnan Uplift
Yabei Sag
Yacheng Uplift
Yanan Sag
Yanan Uplift
Ledong-Lingshui Sag
Beijiao Sag
Beijiao Uplift
W1
W2
W3
W4
W8
W13
Lingnan Uplift
Yinggehai Basin
Ganquan Sag
Xisha Uplift area
Huaguang Sag
Sag
Uplift
W1 Well
Gas field
(c)

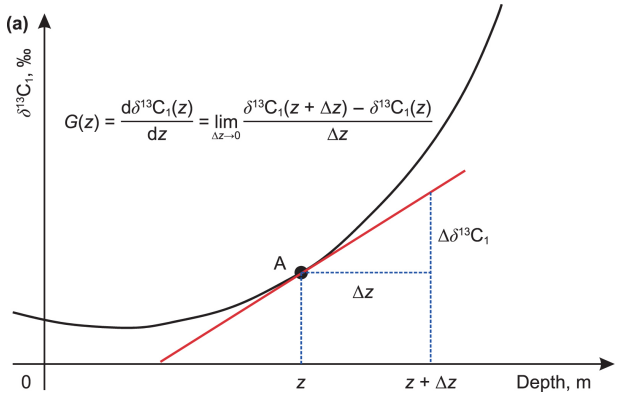

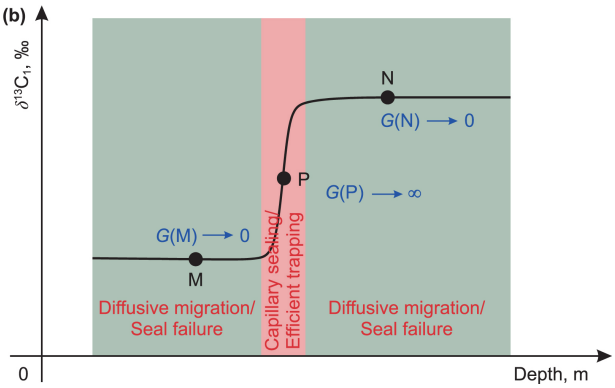

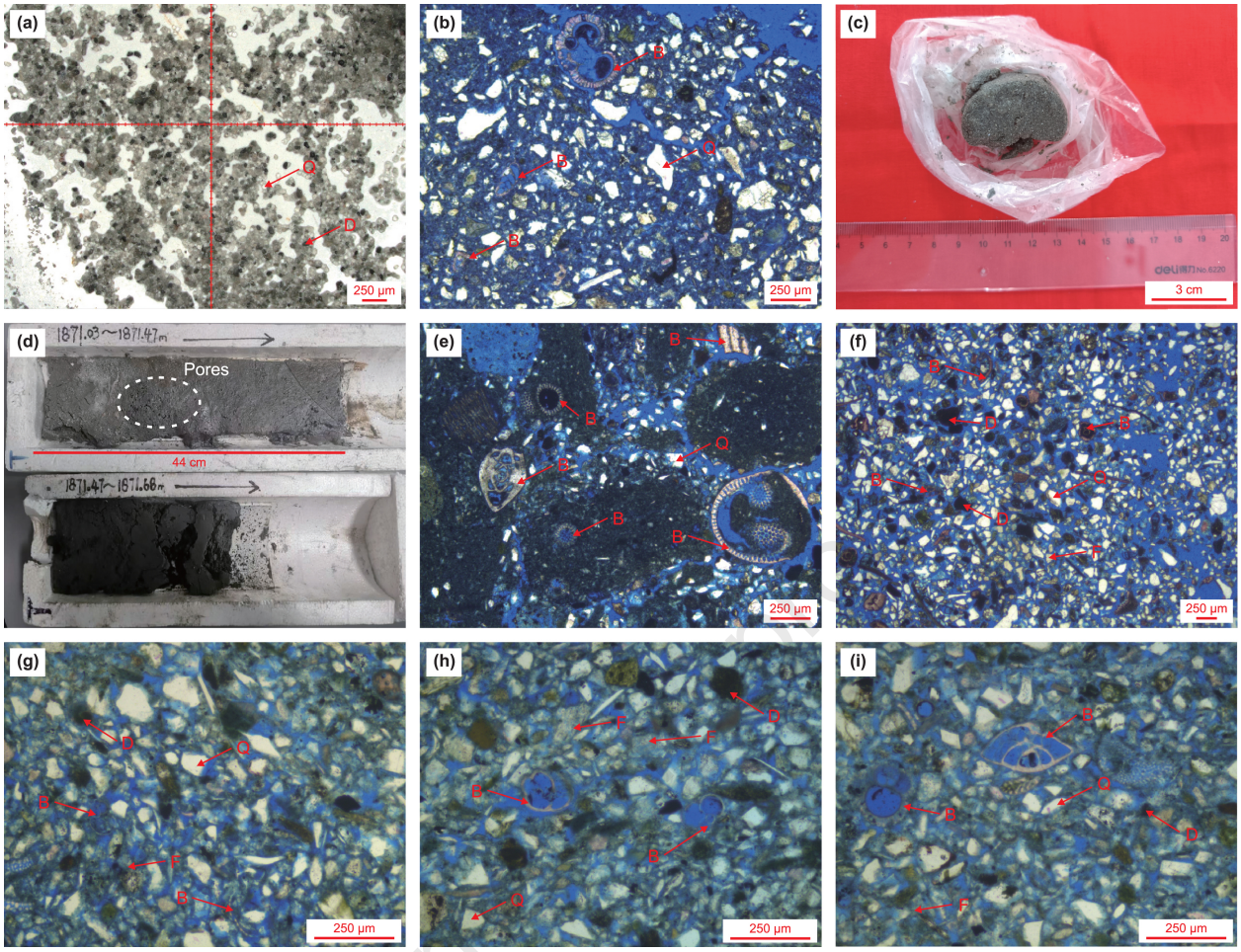
(a)
Q
D
250 μm
(b)
B
B
Q
B
250 μm
(c)
3 cm
(d)
1871.03~1871.47m
Pores
44 cm
1871.47~1871.68m
(e)
B
B
Q
B
B
B
250 μm
(f)
B
D
B
B
Q
D
F
250 μm
(g)
D
Q
B
F
B
250 μm
(h)
D
F
F
B
B
Q
250 μm
(i)
B
Q
B
D
F
250 μm

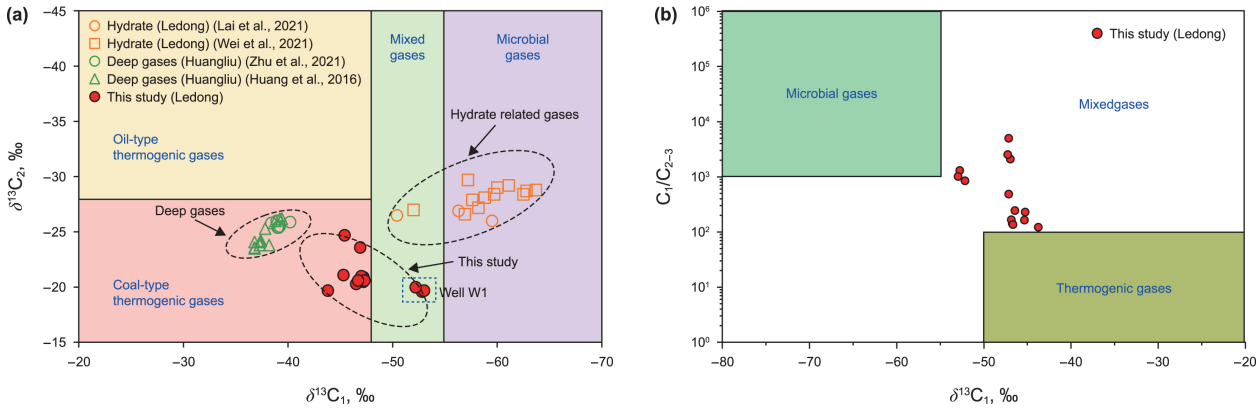

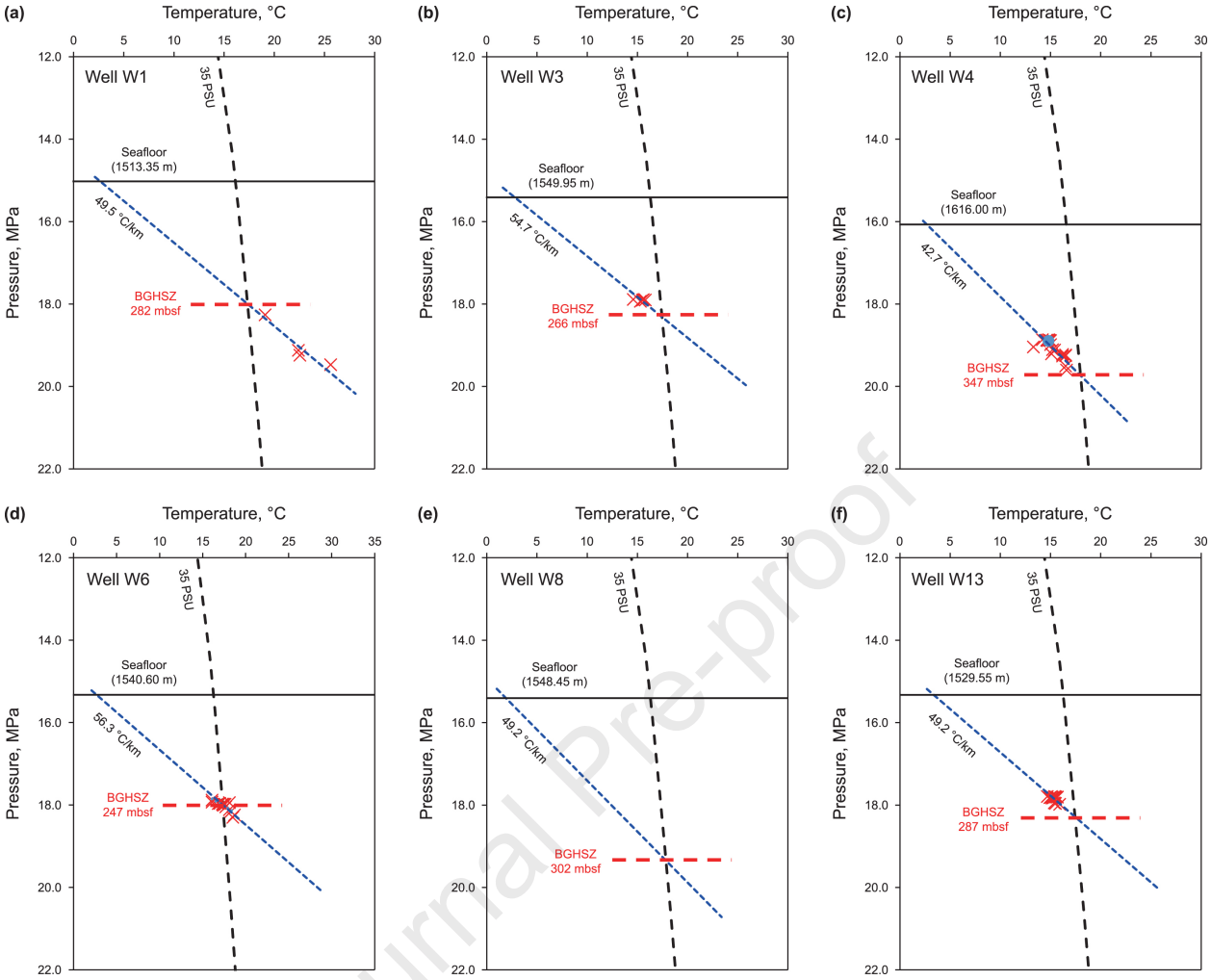

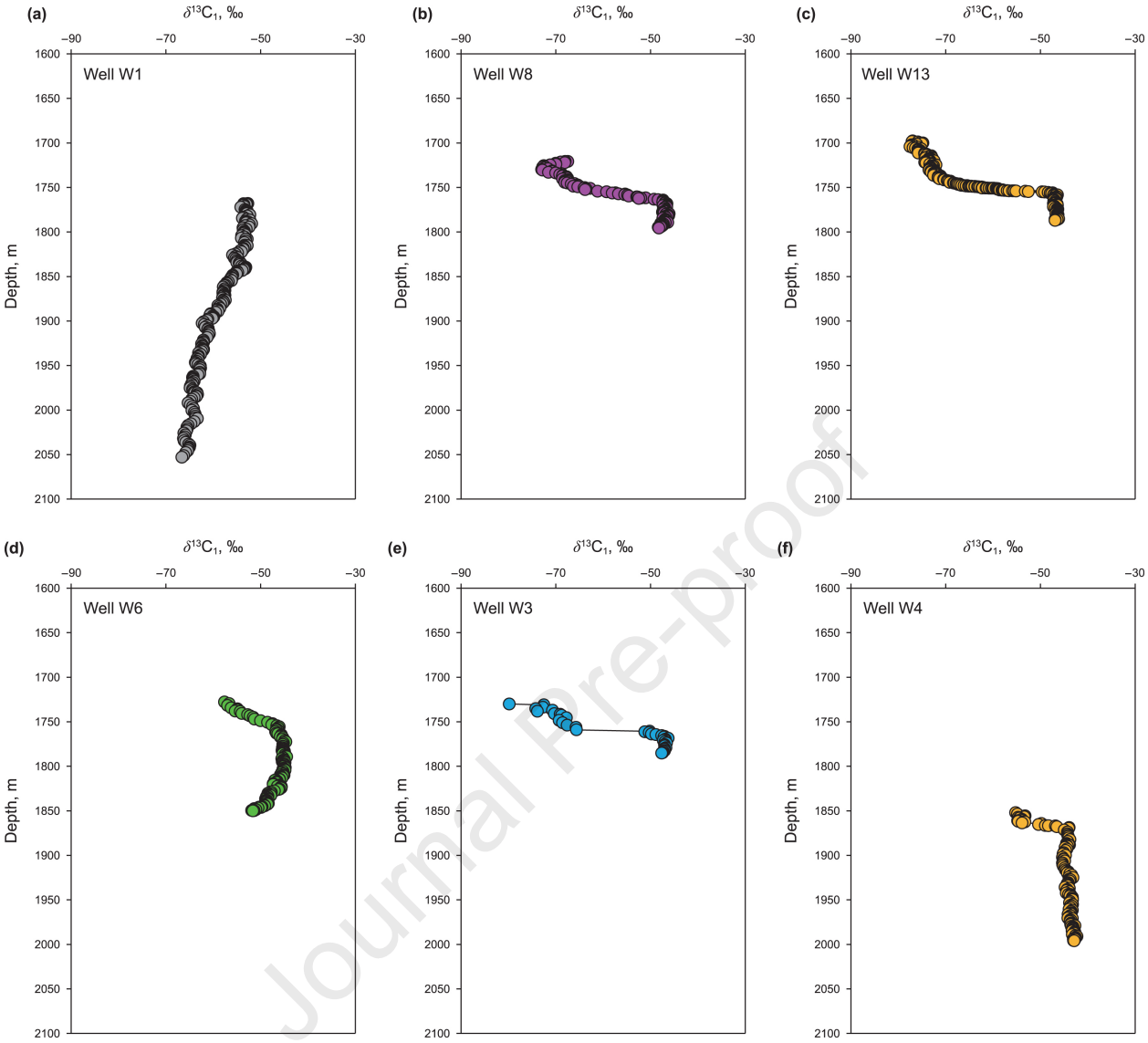

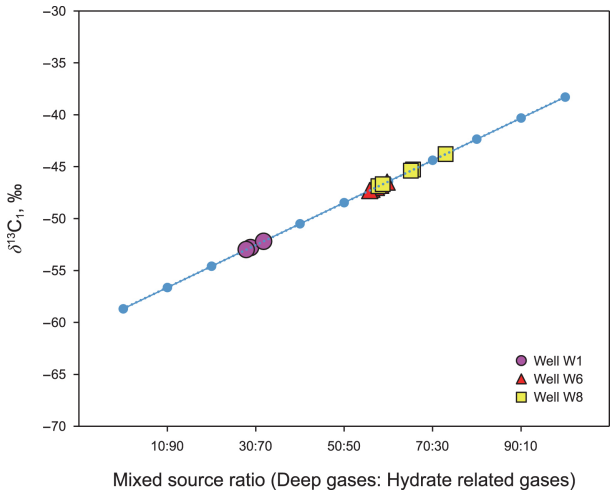

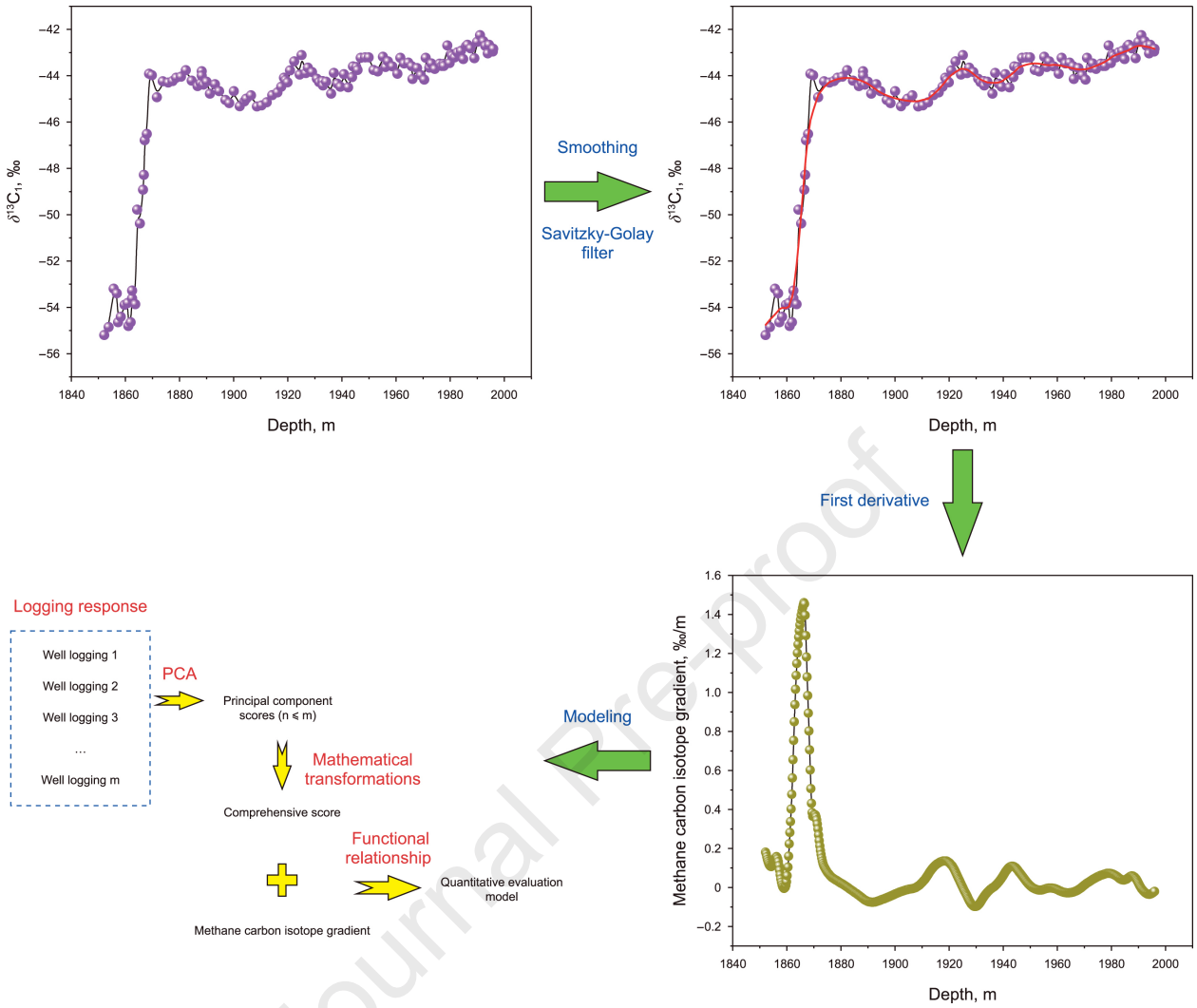

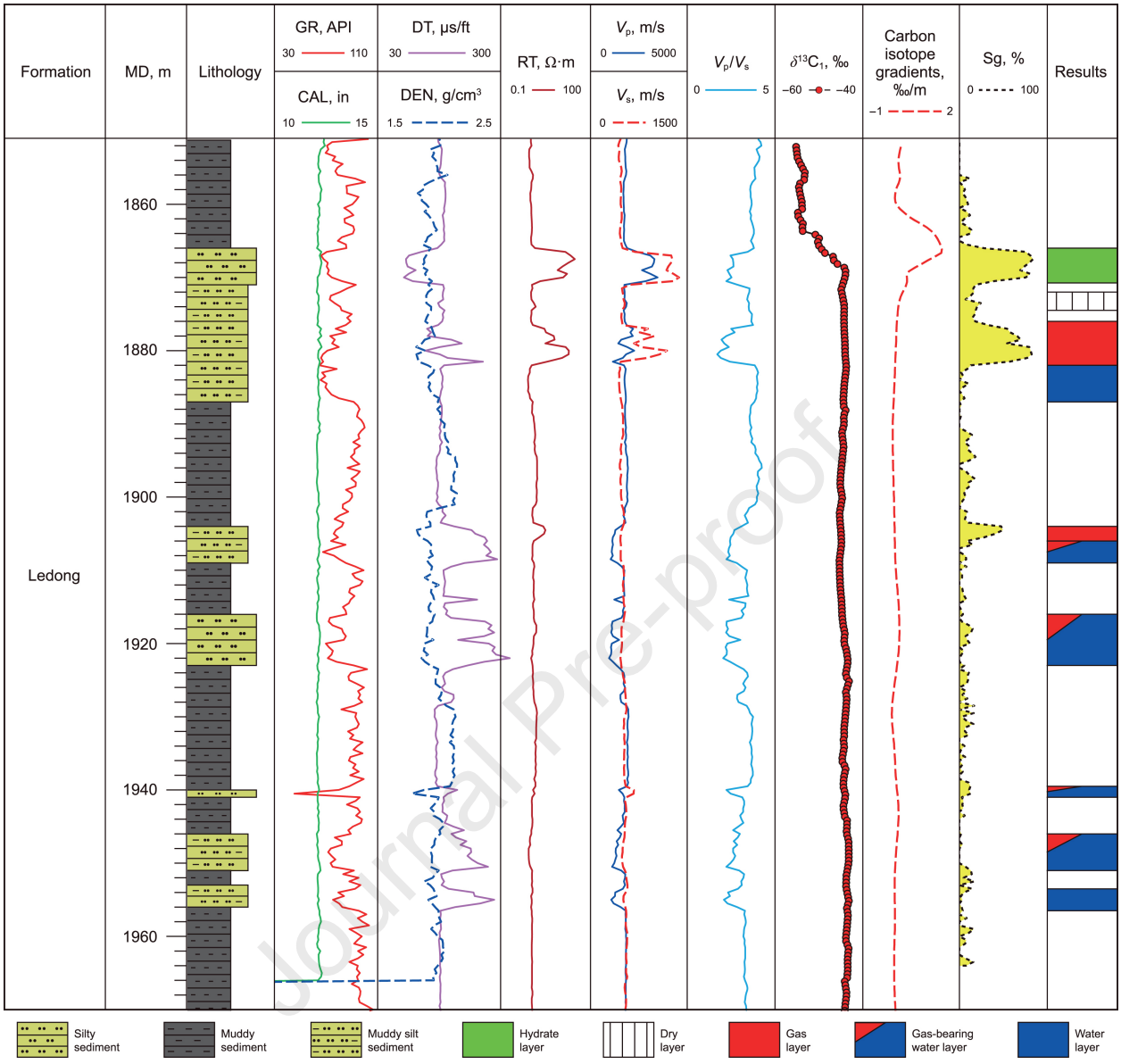

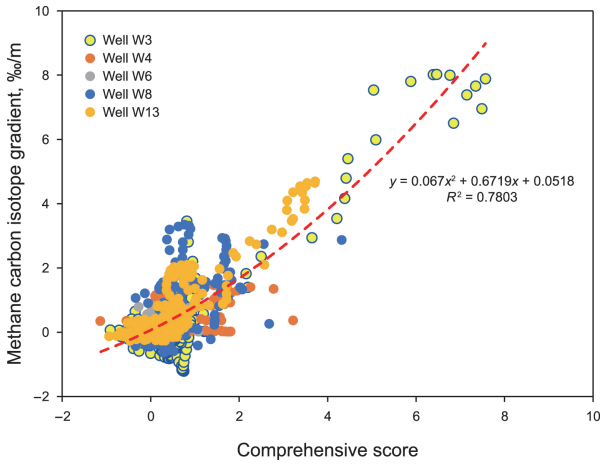

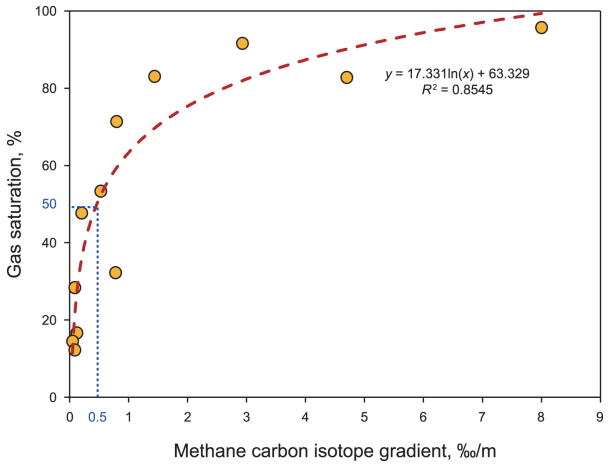

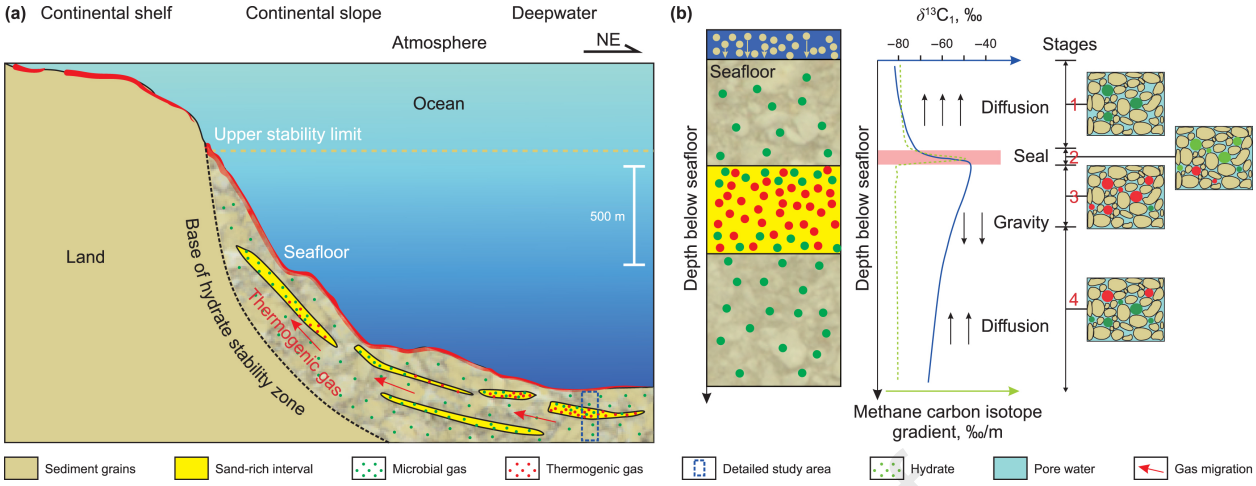

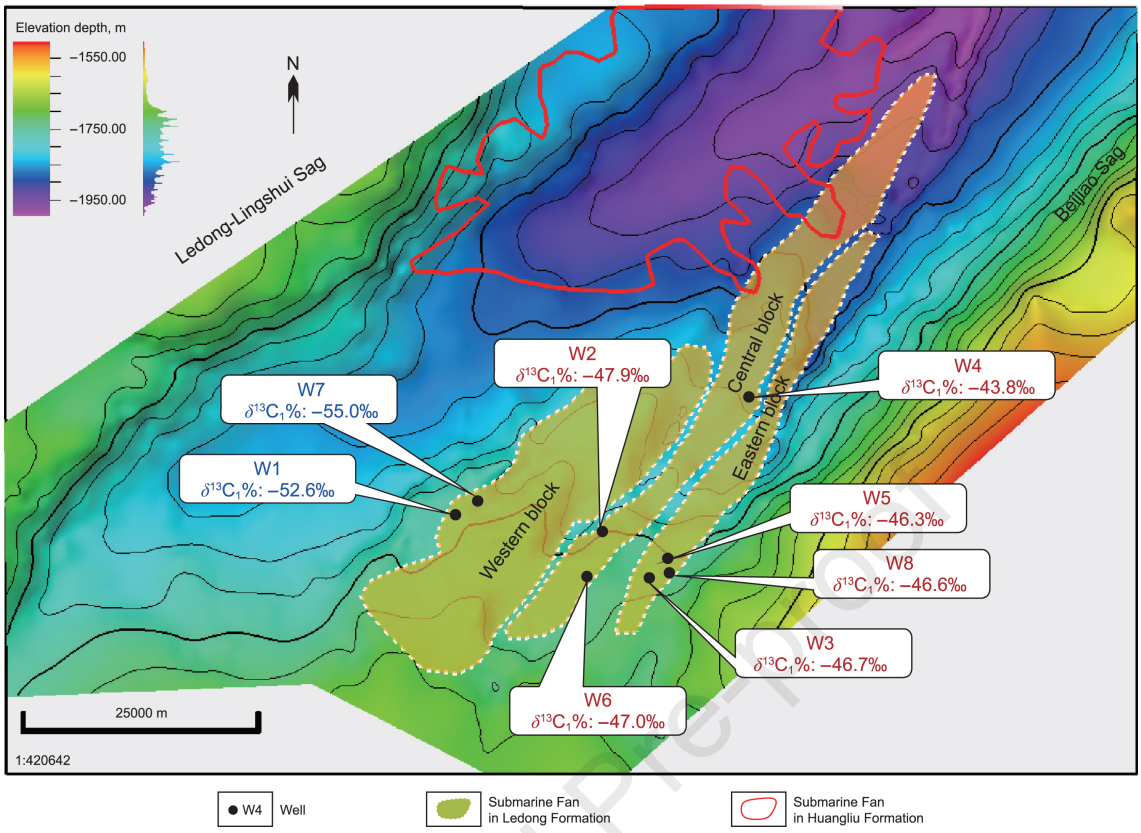

Declaration of interests

☒ The authors declare that they have no known competing financial interests or personal relationships that could have appeared to influence the work reported in this paper.

☐The authors declare the following financial interests/personal relationships which may be considered as potential competing interests: